DTU Library

Fatigue testing of a 14.3 m composite blade embedded with artificial defects – damage growth and structural health monitoring

Chen, Xiao; Semenov, Sergei; McGugan, Malcolm; Madsen, Steen Hjelm; Yeniceli, Süleyman Cem; Berring, Peter; Branner, Kim

[Link back to DTU Orbit](#)

Journal Pre-proofs

Fatigue testing of a 14.3 m composite blade embedded with artificial defects – damage growth and structural health monitoring

Xiao Chen, Sergei Semenov, Malcolm McGugan, Steen Hjelm Madsen, Süleyman Cem Yeniceli, Peter Berring, Kim Branner

Please cite this article as: Chen, X., Semenov, S., McGugan, M., Hjelm Madsen, S., Cem Yeniceli, S., Berring, P., Branner, K., Fatigue testing of a 14.3 m composite blade embedded with artificial defects – damage growth and structural health monitoring, *Composites: Part A* (2020), doi: https://doi.org/10.1016/j.compositesa. 2020.106189

Fatigue testing of a 14.3 m composite blade embedded with artificial defects – damage growth and structural health monitoring

Xiao Chen*, Sergei Semenov, Malcolm McGugan, Steen Hjelm Madsen, Süleyman Cem Yeniceli, Peter Berring, Kim Branner

Department of Wind Energy, Technical University of Denmark, Frederiksborgvej 399, 4000 Roskilde, Denmark

*Corresponding author: xiac@dtu.dk

Abstract: Understanding fatigue damage growth of composite wind turbine blades is an essential step towards reliable structural health monitoring (SHM) and accurate lifetime prediction. This study presents a comprehensive experimental investigation into damage growth within a full-scale composite wind turbine blade under fatigue loading. The blade has artificial defects embedded to initiate damage growth. The damages are detected and monitored using Infrared (IR) thermography, Digital Image Correlation (DIC), and Acoustic Emission (AE). Steady damage growth and imminent structural failure are identified, demonstrating the effectiveness of these techniques to detect subsurface damages. New experimental observations include cyclic buckling of a trailing edge region and tapping and rubbing between the shear web and spar cap, both damages due to adhesive joint debonds. These observations highlight the necessity and the complexity of reliable modeling of nonlinear structural behavior on a large scale in order to predict local fatigue crack growth.

Keywords: wind turbine blade; delamination; fatigue test; damage detection; structural health monitoring; defect

1. Introduction

Having robust, reliable and easy-to-use methods to detect damage growth can save the life of many blades and help extend the life of even more. Wind turbines are designed to have a service life of 20 years or more. Good fatigue performance is undoubtedly important to structural integrity and longevity of rotor blades which are one of the most critical components in the entire wind turbine. Full-scale fatigue testing is mandatory for blade certification [1] and it can be used to determine the fatigue performance of blades that are built with new structural designs, material systems, and manufacturing techniques. Most full-scale fatigue tests of rotor blades have been conducted commercially. Due to confidentiality, the observed failure modes and the underlying mechanisms are not usually published. Among the limited publically available literature, full-scale fatigue tests are investigated tunneling cracks in adhesive joints [2], delamination in the blade root [3], adhesive joint debond between spar cap and shear web [4], and structural degradation in terms of bending stiffness, natural frequencies and damping ratios [5]. The investigated damages are initiated naturally during the fatigue test and are typically not known beforehand. These observed damages are blade specific and might only be relevant to particular blade designs. It is well known that rotor blades, despite different structural designs, show typical damage types such as delamination, adhesive joint debonding, skin/core debonding, and surface cracking, some of which are caused by manufacturing-induced defects, e.g., laminate wrinkles, and can lead to catastrophic blade fracture [6]. The effects of defects in wind turbine blades have been studied extensively under static loading on a relatively small scale using coupons and components but less so under fatigue loading especially on a large scale [7][8][9][10][11][12].

It needs to be mentioned that rotor blades are unavoidably built with defects, however it is damages that result from these defects, rather than the defects themselves, that should be of primary concern. This was also discussed in [13], where a methodology for reliable design and maintenance of wind turbine rotor blades was proposed using a condition monitoring approach and a damage tolerance index coupling the material and structure. In order to study fatigue behavior of typical damages in full-scale blades, artificial defects can be designed and embedded in the blades to initiate the damages of interest. By doing so, the locations and types of damages are known beforehand, and thus suitable nondestructive testing (NDT) and structural health monitoring

(SHM) techniques and their experimental setups can be prepared before the tests. So far, publications on the fatigue damages initiated by artificially induced defects in the full-scale blades are limited. One notable study is from [14] in which two 8.3 m blades with different defect types intentionally embedded. Digital Image Correlation (DIC), Infrared (IR) thermal imaging, and Acoustic Emission (AE) were used in that study to identify damages during the tests. In the report [14], however, these measurement results were not reported, and mainly the photos of the blade after the final failure were provided. Another study [15] worthy of note is a full-scale fatigue test on a 9 m blade embedded with laminate wave defects. Various SHM techniques were used to detect the defects and track the resultant damage, focusing on the damage detection capability of these techniques. Similar exercises were done in [16] on a 9 m blade which was built without any embedded defects, providing an overview of the SHM and NDT system setups and test results. One of the identified challenges was the proper placement of the SHM systems and other diagnostic equipment on the blade as the failure location and mechanism were not known beforehand.

Understanding the underlying failure mechanisms and revealing the unknown damage behavior of the blades, among others, are essential purposes of blade testing. To achieve that, not only must a delicate blade test with proper instrumentation and measurements be conducted, but accurate interpretations of the experimental observations and their implications to future blade design and testing must also be concluded. These tasks require identifying damages and tracking their growth when the blades are subject to fatigue loading. Motivated by the aforementioned, this study conducts a comprehensive experimental investigation on fatigue damage growth in a full-scale composite blade embedded with artificial defects. Particular considerations are placed on the blade testing, damage identification and monitoring, and result interpretations and implications. First, different types of artificial defects are designed and intentionally placed in the blade during manufacturing to trigger typical damages of interest in the full-scale blade fatigue test. In total, four types of artificial defects have been included in the blade at multiple sites. The types are laminate wrinkles in spar caps, core materials/skin laminates debonds in sandwich panels, adhesive joint debonds in trailing edge, and adhesive joint debonds between the shear web and the spar cap. The defects are designed based on experimental results from a previous test campaign on another 14.3 m blade of the same type, which has no embedded artificial defects and the preliminary fracture mechanics-based finite element simulations. The test campaign includes four static loading directions and two fatigue loading directions following IEC 64100-23 [1]. Second, a combination of NDT and SHM techniques, namely DIC, AE, and IR thermography, is used for real-time, large-area, remote damage detection and monitoring. Moreover, the implications of experimental setups in the laboratory to the field application are addressed. Finally, observed nonlinear structural behavior in the damage regions is discussed in detail, shedding light on accurate numerical modeling and prediction of damage growth in large scale composite rotor blades under fatigue.

As such, the significance and novelties of this work are:

- Presenting a comprehensive and detailed experimental investigation on fatigue damage growth of a full-scale composite wind turbine blade with artificial defects intentionally embedded.
- Revealing new nonlinear structural phenomena not publically studied before but important for accurate numerical modeling of the fatigue damage growth on a large scale.
- Demonstrating real-time, large-area, remote damage detection and monitoring of a full-scale blade under fatigue loading using a combination of various NDT and SHM techniques.
- Detailing defect design, manufacturing as well as experimental setups, providing essential information to the research community to reproduce our findings in the laboratory and to facilitate effective SHM application in the field.

The following Section 2 describes the blade with the embedded artificial defects including defect design and manufacturing. The experimental setup of the full-scale blade test under flapwise and edgewise fatigue loading is presented in Section 3. Section 4 presents and discusses results from NDT and SHM of the flapwise and the edgewise fatigue test, sequentially. Based on these findings, Section 5 summarizes the major conclusions and outlooks of this study. Complementary details related to this work are provided in Supplementary material.

2. The blade with embedded defects
2.1 The blade

A 14.3 m wind turbine blade is tested in the study. The blade is made of fiberglass/polyester composite materials and has two shear webs bonded to spar caps. The blade is unpainted. Unidirectional (UD), bi-axial (BIA) and tri-axial (TRI) laminates, chopped fiber mats (Chop), and PVC foams were used to manufacture the blade. The geometry and detailed material properties are proprietary. The normalized material properties used in the blade are shown in Table 1.

Table 1 Material properties of fiberglass/polyester composites and PVC foam used in the blade[*]

Material	E_{11}	E_{22}	E_{33}	G_{12}	G_{13}	G_{23}	u_{12}	u_{13}	u_{23}
UD	1.00	0.35	0.35	0.12	0.12	0.12	0.24	0.09	0.48
BIA	1.00	1.00	1.00	0.83	0.83	0.49	0.53	0.19	0.02
TRI	1.00	0.66	0.66	0.42	0.42	0.31	0.48	0.01	0.08
Chop	1.00	1.00	0.54	0.35	0.16	0.16	0.32	0.20	0.35
Foam	1.00	1.00	1.00	0.36	0.36	0.36	0.40	0.40	0.40

*All moduli are normalised by E_{11}. Poisson's ratios are the original values without normalization. Subscripts 1, 2 and 3 mean longitudinal, transverse and through-thickness direction, respectively.

The blade used in this study is newly made and has not been tested. It is worth noting that in a previous study [17] a 14.3m blade that has the same design as the current one but has no embedded defects has been tested under standard static and fatigue loading following IEC 64100-23 [1]. The structural performance of this type of blades has been studied and the experimental results are used as a reference when designing the defects and the test plan.

2.2 Defect design

Composite structures are unavoidably built with defects. Nevertheless, not all defects lead to growing damage under fatigue loading. Defects can have different shapes and characteristics, which may lead to different damage severity if they grow. When designing the defects in the blade, we have a few key considerations. First, the type of defects should be typical and relevant to blade structures; second, the defects should initiate damage that grow under fatigue load. Third, the defects should be well documented and easy to reproduce by other research.

In total, four types of defects are designed to be included in the blade. They are laminate wrinkles in spar caps, core materials/skin laminates debond in sandwich panels, adhesive joint debonds in trailing edge, and adhesive joint debond between the shear web and the spar cap. These defects are among the most typical types of defects found in wind turbine blades [9][18][19]. The overview of the defect distribution over the blade is schematically presented in Fig. 1. The detailed descriptions of the defects are shown in Table 1.

Fig. 1. Distribution of artificial defects and sensors over the blade. Defect types: wrinkle insert – WK; sandwich skin/core debonding – SD; trailing edge adhesive joint debond – TD; shear web/spar cap debond – WD. Sensor types: strain gauge – SG; Acoustic emission sensor – AE. (a) The distribution of defects and sensors over the pressure side shell and trailing edge of the blade. (b) The adhesive joint debonds between the rear shear web and the spar cap at the suction side of the blade.

Table 1. The detailed descriptions of defects that are embedded in the blade to be tested under fatigue

Defect	Chordwise length (cm)	Spanwise location (m)	Through-thickness layup location	Description
WK#1	33	7.3	$[TRI]_2[UD][\mathbf{WK}][UD]_{14}[TRI]_2$	Casted resin inserts to create a wrinkle in the spar cap laminate on the pressure side of the blade.
WK#2	31	8.3	$[TRI]_2[UD][\mathbf{WK}][UD]_{12}[TRI]_2$	
WK#3	28	9.3	$[TRI]_2[UD][\mathbf{WK}][UD]_9[TRI]_2$	
WK#4	26	9.8	$[TRI]_2[UD][\mathbf{WK}][UD]_8[TRI]_2$	
SD#1	30	2.5-2.9	$[TRI]_2[\mathbf{SD}][Foam][TRI]_2$	Slip foils to create a debond region between cores and skin laminate on the pressure side of the blade.
SD#2	30	3.8-4.2	$[TRI]_2[\mathbf{SD}][Foam][TRI]_2$	
SD#3	15	5.4-5.6	$[TRI]_2[\mathbf{SD}][Foam][TRI]_2$	
TD#1	20	5.8-7.0	$[TRI]_4[Adhesive][\mathbf{TD}][Adhesive][TRI]_4$	Slip foils to create a debond region of trailing edge adhesive bondline.
TD#2	20	8.3-9.5	$[TRI]_4[Adhesive][\mathbf{TD}][Adhesive][TRI]_4$	
WD#1	2-3	1.00-1.65	*Not applicable*	Adhesive joint debonds between the shear web and the spar cap on the suction side.

The locations and the sizes of the defects are determined based on experimental results from reference static and fatigue tests of this type of blades and preliminary finite element simulations using a fracture mechanics based approach, which will be presented in a separate study. A few considerations are as follows: wrinkles are usually found in thick laminates, e.g., spar cap and blade root, and in the regions with large curvature changes, e. g., root transition regions. It is decided to embed four wrinkles in the spar cap where a cyclic stress level is high from 7 to 10 m blade spanwise, damage inspection is practically easy to carry out and numerical modeling in a future study is straightforward and relatively simple to perform. The locations of sandwich debonding are determined considering that the aft panel, especially the one close to the maximum chord, is subject to cyclic buckling when the blade is under fatigue loading and would most likely to trigger damage growth if the debonding defects are placed there. In addition, this blade has no sandwich construction in the leading edge panels, leaving the aft panels the only regions to include debonding defects in sandwich panels. Two trailing edge debonds are placed in the regions where the trailing edge is under high cyclic stress under fatigue loading, i.e., from 6 to 7 m and 8 to 9 m spanwise. The cyclic stress distributions along the blade length under fatigue loading are presented in section 3.3.

2.3 Defect manufacturing

Four resin inserts are embedded in the spar cap laminate to create out-of-plane wrinkles. The resin inserts are cast in a mold that is milled from an EB700 high-temperature epoxy tooling board, see Fig. 2. The resin inserts have a wave height of 4 mm and a width of 40 mm. The wave profile, provided in Supplementary material, is designed in such a way that the tangent line to the bottom wave curve coincides with the longitudinal direction of the spar cap laminates. A resin inlet and two air outlets are designed to facilitate the casting process. The polyester resin used to cast the inserts is the same as the one used to build the blade. Once the resin inserts are manufactured, they are placed in the spar cap between UD fiber fabrics according to the through-thickness layup locations specified in Table 1. The resin inserts and fiber fabrics are resin-infused assisted by vacuum, finally producing a pressure side shell of the blade with four wrinkles embedded in the spar cap laminate, see Figure 3.

Fig. 2. A mold used to cast resin inserts to be embedded in the spar cap laminates to create out-of-plane waviness, i.e., wrinkles. (a) The design of the mold and the resin insert, dimension in mm. (b) The actual mold parts fabricated by milling an EB700 high-temperature epoxy tooling board. (c) Casting the resin insert by injecting resin into the resin inlet. Two air outlets are also made in the mold to facilitate casting. Fiberglass composite plates are glued on two mold parts to provide stiffness to the mold.

Fig. 3. Manufactured pressure side spar cap embedded with four resin inserts to create wrinkles in the laminate. (a) The overview of four wrinkles with embedded resin inserts in the entire spar cap. (b) A close up of WK#3. The resin inserts are embedded in such a way that the flat side of the inserts is placed towards the mold side, i.e., the outside surface of the blade, and the bump side is facing the inside surface of the spar cap. The outside surface of the blade after demolding is therefore smooth.

It is well known that wrinkles in laminates can have various shapes and topologies. Trying to represent large varieties of wrinkles using one single shape is an impossible task. Considering that the primary focus of this study is damage growth and the purpose of embedding wrinkles is to trigger growing delamination, the current winkle shape is chosen as it is very general and can be described easily with a wave amplitude versus a wavelength ratio 1/10, which has been found in a 50 m long commercial wind turbine blade.

To create debond regions between core materials and skin laminates in sandwich panels, slip foils, or perforated release films R120-P3, with a thickness of 28 μm are inserted at the interface of interest. The slip foils are divided into two parts: the center part is made by the original slip foils to create a fully debonded region while the outskirt part is made by perforating the slip foils with holes with a diameter of 10 mm to create a partially bonded region, see Fig. 4. The purpose of including this partially bonded region is to facilitate the progress of debonding during the fatigue test. Preliminary FE simulations indicate the debond is unlikely to grow under pure flapwise or edgewise fatigue loading of the blade. Note that an area of dry fiber fabrics arises in the center of the debond region due to the lack of resin flow in this area.

Fig. 4. The debonding SD#1 was introduced by inserting a slip foil between cores and skin laminates. The slip foil is made in such a way that the center region creates a full debond while the outskirt creates a partial debond due to perforations (holes with D=10mm) made in the slip foil. An area of dry fiber fabrics arises in the center of the debond region due to the lack of resin during the blade manufacturing.

Moreover, two pieces of slip foil with a length of 1.2 m and a width of 20 cm are placed on top of the adhesive bond line along the trailing edge before the two blade shells are glued to form an entire blade. The adhesive joint debonds between the rear shear web and the spar cap on the suction side of the blade are created during blade manufacturing with an initial debond length measured to be approximately 65 cm as sketched in Fig. 1(b).

It is worth noting that using slip foils to create artificial debonding in sandwich panels and adhesive joints is a commonly used technique although it does not necessarily generate very realistic debond defects. Admittedly, creating a realistic debond defect, or any other defects, using any artificial methods is still a challenging task due to the sheer complexity of the manufacturing process which involves many interplay factors including multi-physics, material systems, layup design and even technician skills. In this study, we used slip foils to create material separation and represent a debond status so that neither normal tensile stress nor shear stresses can be transferred – a close approximation of physical conditions in a debond region. Therefore, it is regarded that the artificial defects introduced in the blade are representative enough for the purpose of this study.

3. Experimental setup
3.1 Instrumentation

The blade is mounted on a test stand and about 2 m above the ground. The blade is instrumented with strain gauges HBM 1-LY61-10/350 using a Z70 glue. They measure longitudinal strains of two spar caps, the leading edge and the trailing edge along the blade axis at three cross sections, i.e., 7 m, 9 m, and 10 m, Fig. 1(a). A sampling rate of 20 Hz is used to collect strain gauge data by a Gantner data acquisition (DAQ) system.

An acoustic emission (AE) measurement system was used during the testing of this blade. The Sensor Highway III by Physical Acoustics is a multichannel system suitable for long term monitoring in the field. PK15I sensors are used which are resonant at higher frequencies (150 kHz) and give a good localized response from polymer composite material failures. The sensors of interest in this study are ch #1 mounted on the spar cap near the root of the blade, ch #6 and #7 mounted on the trailing edge of the blade, and ch #8 and #9 mounted internally by the spar cap close to the debond crack front towards the blade tip direction. The distribution of AE sensors is shown in Fig. 1.

Two non-contact damage identification methods, namely Infrared (IR) thermography and Digital Image Correlation (DIC), are used during the fatigue test. Previous studies [20][21][22] have used these two methods to detect damage of rotor blades subjected to fatigue. This study further explores the application of these two methods to full-scale blade tests under fatigue loading focusing on the nonlinear structural behavior of the damaged regions.

Thermal images of the blade are taken remotely, i.e., 9.3 m above the ground to detect thermal abnormities under fatigue loading. The regular optical images are also taken by the regular camera placed at the same location as the thermal camera. Fig. 5(a). The thermal camera FLIR A655SC is used in this study. The camera has an uncooled microbolometer detector with a resolution of 640 × 480 pixels and a pitch of 17 μm. The accuracy of measurement is ±2°C or ±2% of reading. The thermal sensitivity measured by noise equivalent temperature difference (NETD) is < 30 mK. The field of view (FoV) is 25° × 19°.

A DIC measurement system is mounted on a scaffold tower close to the blade to carry out non-contact damage detection, Fig. 5(b). The GOM ARAMIS system with two 12 MP cameras and 24 mm lenses are used to perform DIC measurements. Two cameras with a 600 mm distance in between are mounted on an aluminum bar. The distance from the DIC system to the blade is about 900 mm and the field of view is about 700x700 mm and the depth of view 600 mm. The calibration is performed before the test following the standard procedure specified by the equipment producer. A 700 mm carbon fiber cross is used in the calibration procedure. The calibration error is within 0.029 pixels.

Two local regions are of interest from the DIC measurement. The first region is the spar cap embedded with a wrinkle WK#2 at 8.3m, where randomly distributed speckles with a diameter ranging approximately from 1 to 2mm and a fill density of 60% are painted. The second region is the trailing edge embedded with a debond

TD#1 from 5.8 m to 7.0 m, where a polymer foil printed with a randomly distributed speckle pattern is glued to the trailing edge region of interest. The speckle pattern is generated by Speckle Generator [23] with a diameter of 1 mm, a fill density of 75% and a variation of 75%. The DIC measurements are recorded with a 58 frame/sec (FPS) rate and few strain gauge signals are captured for synchronization purposes.

Fig. 5. Experiment setup of the full-scale blade fatigue test. (a) An IR thermal camera is placed 9.3m above the ground to overview thermal abnormities generated in the blade. A scaffold tower is used to mount the DIC cameras for damage identification in the spar cap embedded with wrinkles during the flapwise fatigue loading. (b) DIC measurements of the trailing edge region during the edgewise fatigue loading.

3.2 Fatigue exciter

A loading saddle is mounted at a 5.2 m cross section to connect a ground-based fatigue exciter for loading. A dual-axis fatigue exciter, developed by R&D A/S within the project BLATIGUE, is used in this study. The exciter is an electro actuated ground-based exciter constructed for fatigue testing of wind turbine blades. It is a backlash constrained dual-axis exciter. It applies controlled dynamic forces to the blade driving it into oscillating motion. Forces are applied in a flap- or edgewise direction or as a combination of the two. The actuation is procured by hollow shaft permanent magnet synchronous machines. Two gears are mounted on each machine in a pre-tensioned mechanical loop constraining backlash in the gearboxes. Torque arms are mounted on the output shaft side of the gears and deliver forces to push rods via rod end link bearings. Push rod top end link bearings are attached to a common axle and direct forces into a loading saddle attached to the blade, see Fig. 5. The exciter has a force capacity of ±10 kN in flapwise direction and ±3 kN in edgewise direction. The displacement amplitude capacity is 0.125m in flapwise direction and 0.05m in edgewise direction. The excitation frequency capacity is from 0.15 to 10 Hz.

3.3 Fatigue test

The fatigue test is carried out under flapwise fatigue loading and edgewise fatigue loading subsequently. The exciter drives the blade into resonance vibration. The bending moments applied to the blade under fatigue are calculated using a test simulation tool developed by DTU Wind Energy as shown in Fig. 6, see Supplementary material, The flapwise fatigue test is carried out with an excitation frequency of 2.30 Hz and a total cycle number of 38,000 while the edgewise fatigue test is carried out with an excitation frequency of 4.65 Hz and a total cycle number of 273,000. The resulting strain distributions along the blade under fatigue loading are calculated and compared with strain gauge measurements during the test as shown in Fig. 7.

In the flapwsie fatigue test, a strain range 3800 με at the 9 m spar cap at the pressure side of the blade is used as a test control strain. In the edgewise fatigue test, there are two loading levels. The test control strain is 1800 με in the 10 m leading edge in the first load level and 2200 με in the second. Fatigue tests are interfered with several stops for blade inspection. The blade is repaired before starting the edgewise fatigue test due to severe damage caused by the flapwise fatigue test.

Fig. 6 Bending moment distributions of the blade under fatigue loading. The exciter is mounted at the 5.2 m section and loads the blade to resonance vibration under flapwise and edgewise loading, respectively.

Fig. 7. Strain distributions along the blade under fatigue loading with a comparison between theoretical calculations shown as curves and measurement data shown as markers. (a) Stains along with spar caps of the blade under flapwise fatigue loading. (b) Strains along trailing edge and leading edge of the blade under edgewise fatigue loading.

4. Results and discussion

4.1 Flapwise fatigue

Delamination growth

During the flapwise fatigue test, several damages initiate and progress from artificial defects. The most significant is the delamination originated from laminate wrinkles embedded in the spar cap. Fig. 8 shows three locations at 7.3 m, 9.3 m, and 9.8 m which have visible delamination growth with the increase of the fatigue cycle number. It is visual as the blade is not painted in these regions. It can be seen that the delamination regions at these three locations exhibit a similar belly shape at both sides of the embedded wrinkles. The center regions show maximum delamination growths as they are subject to higher cyclic strains due to the curvature of the spar cap in the transverse direction, i.e., meaning that the central regions are furthest away from the neutral axis of the cross sections when the blade is under flapwise fatigue loading. Different stages of delamination growth are marked with the increase of fatigue cycle numbers up to 38000 cycles under high-load fatigue. Note that the delamination at 8.3 m is not visible due to the paint for DIC measurements.

Fig. 8. Delamination growth in the spar cap under flapwise fatigue. The delamination is initiated by embedded wrinkles in the unidirectional laminates of the spar cap. The original wrinkles are marked in green. The delamination areas at 7.3 m, 9.3m, and 9.8 m are identified with red curves marking 6000 cycles, black curves marking 18600 cycles and blue curves marking 38000 cycles. The delamination at 8.3 m is not marked as it is invisible due to the paint with speckle patterns for DIC measurements. The delamination at 8.3 m is inspected after the paint is removed after the fatigue test at 38000 cycles.

The relationship between delamination growth areas and the fatigue cycle number in three locations is shown in Fig. 9. It can be seen that the delamination areas grow steadily at 9.3 m and 9.8 m with a rate of about 0.18 mm^2/cycle over the entire flapwise fatigue test. The delamination area at 7.3 m grows with a rate of 0.22 mm^2/cycle at a starting stage of the test and the growth rate speeds up to 0.43 mm^2/cycle at a later stage. These growth rates are important values to be compared with numerical models which will be presented in a separate study.

Fig. 9. The relationship between delamination growth areas and the fatigue cycle number in three locations. The increased delamination areas are measured by integrating delamination fronts which are curve fitted with splines. It shows the stable delamination growth at 9.3m and 9.8 m locations and a rapid increase of a delamination speed at the 7.3 m location quantified by $\Delta A/\Delta N$.

It should be mentioned that the delamination damage is observed from the blade surface. After the blade test, a post-mortem investigation is conducted by cutting the delaminated regions. It is found that the delamination has progressed not only along the blade length direction but also through the laminate thickness direction – meaning that there are multiple delamination cracks at different locations in the damaged regions. This damage phenomenon is similar to the observation found in a spar cap laminate of an in-service commercial blade studied in [6]. Delamination cracks interact with each other and compete for damage growth under fatigue loading. Modeling this complicated damage phenomenon requires extensive efforts using numerical approaches. A possible pathway is to first identify or assume initial crack location(s); second, calculate energy release rates at crack tips and corresponding growth rates; and then extend the crack length and/or add new cracks; after that, calculate energy release rates at new crack tips and eventually iterate the process until crack lengths exceed the predefined values or a failure occurs. In this work, we only focus on experimental investigations due to the scope of the study. The high-quality and well-documented experimental data can be used in a future numerical study.

Thermal imaging

The delamination growth under fatigue loading generates significant thermal footprints as shown in Fig. 10. It can be seen that four locations heat up including the one covered with the paint at 8.3 m. Actually, the delamination at 8.3 m shows the most significant thermal footprint among four locations. Comparatively, the locations at 9.3 m and 9.8 m show a much smaller size of thermal footprints. Although it cannot be determined through visual inspection how large the delamination area is at 8.3 m due to the covered paint for DIC measurements, the thermal image reveals a much larger delamination area at 8.3 m compared to the one that can be seen at 7.3 m, indicating that the spar cap at 8.3m is more damaged than at other three locations.

Fig. 10 Thermal footprints of delamination in the spar cap when the blade is subject to flapwise fatigue loading. The thermal image is taken remotely from 9.3m above the ground at a fatigue cycle number of approximately 30,000. A regular RGB optical image of the blade is also included for comparison. All images are taken when the blade is under fatigue loading.

Fig. 11. Time history records of strains on the pressure side of the spar caps at 7 m and 9 m section about 6 hours before terminating the flapwise fatigue loading. (a) The decay of the strain ranges is obvious with a test control strain at 9 m decreasing from 3800 με to about 3200 με. Multiple test stops are done to inspect the blade and they are also recorded in the strain measurements. (b) The close-up of the last part of strain records before the blade is fractured, showing that the strain ranges increase due to the change of the excitation frequency before they drastically decrease. During this process, significant tapping sounds are generated from the blade. The flapwise fatigue test is subsequently terminated.

Strain range decay

At the late stage of the flapwise fatigue test, it is found that strain ranges on the spar cap reduce gradually over time although fatigue test parameters are kept unchanged, see Fig. 11(a). Multiple test stops are carried out for inspection and no stain gauge malfunction is found. The strain range decay is thought to be caused by the change of dynamic properties, i.e., natural frequency and mode shape, of the blade due to the accumulated damage in the spar cap which is primarily responsible for providing bending stiffness to the blade under flapwise loading. Due to the change of the dynamic properties, the fatigue exciter does no longer excite the blade at its original resonant frequency which then decreases the cyclic strain ranges accordingly. This reasoning is justified by the observation that a slight decrease of the excitation frequency from the original 2.30 Hz to 2.22 Hz increases the cyclic strain ranges as shown in Fig. 11(b) from the time of about 21210 s. Continuing the fatigue loading afterward leads to a significant strain decrease and tapping sounds from the blade. The test is then terminated at 38000 cycles and the blade inspection is carried out subsequently.

The strain range decay also leads to potential modification of our fatigue exciter towards more adaptive and smarter test equipment. This can be achieved by adding a feedback loop to the exciter using signals from an array of accelerometers mounted along the blade. The accelerometer array captures mode shapes and natural frequencies of the blade either in real-time or in intermediate stages during the fatigue test. The exciter uses these measured data to adjust excitation parameters, making sure that the blade is always at its peak resonance in the fatigue test. This exciter modification will be the future work following the BLATIGUE project that funded this study.

Acoustic emission

Acoustic emission is recorded throughout the fatigue test. Only the data of most interest are presented here due to a large number of measurements. Fig. 12 shows scatter plots of AE energy aligned with strain gauge measurements. There are four blocks of data separated by three test stops for blade inspection before the final failure of the blade. The AE energy measurements show that high energy activities occur in Block 1 when the strain range decay starts to appear during the fatigue test, indicating considerable damage builds up in the blade. High energy activities continue to occur in Block 2 and 3 in channel #6 and #7, see Figure 1, which indicates material damage around 8.3 m. Visual inspection has been conducted during the test stops and no damage is found in the trailing edge debond TD#2. At the end of Block 4, a boom of AE energy activities is recorded with very high values in all channels before the test is terminated.

Fig. 12. Scatter plots of AE energy show detected activities before the blade failure with four blocks of activities matching the strain gauge trace. (a) Time history records of strains at 7 m and 9 m section. (b) The overview of AE energy shows a dramatic increase of AE activities right after 21000 s particularly in channel #1, #6 and #7. (c) A close-up zoom view of (b) with AE energy below 1000 MARSE shows that high energy activities occur in Block 1 when the strain range decay starts to appear. Two high energy activities occur in Block 2 in channel #6

and #7, respectively. High energy activities occur at the end of Block 3 where the strain range decay is significant before the blade fails in Block 4 where a boom of AE energy activities is recorded.

A detailed look at the data in Block 4 shows interesting features, see Fig. 13. The AE energy record shows two separate groups of peaks at about 21260 s and 21300 s in ch #1, #6 and #7. Most of the energy peaks are recorded within one minute from 21250 s to 21310 s. The imminent failure of the 8.3 m location can be indicated by the first AE energy peak at 21260 s although no change of strain levels is observed. A significant strain decrease is observed right after the second peak of drastic AE energy as a result of a critical structural failure of the blade.

Fig. 13 Scatter plots of AE energy within Block 4 around the time when the blade fails. (a) Strain time history records at 7 m and 9 m section from 21200 to 21380 s. (b) The AE energy record shows two separate groups peaks at about 21260 s and 21300 s in ch #1, #6 and #7. Note that no change is observed in the strain record when the first peak occurs. A significant strain decrease is observed right after the second peak of drastic AE energy occurs followed by the failure of the blade in its spar cap.

Note that channel #8 and #9 have been active during the fatigue test but they only generate low AE energy per hit with average values of 9.5 and 6.7 MARSE/hit, respectively. In comparison, ch #1, #6 and #7 generate 215.8, 37.0, and 150.5 MARSE/hit, respectively. Visual inspection reveals that the low AE energy activities in ch #8 and #9 are caused by the tapping, or cyclic contact, between the shear web and the spar cap on the blade suction side shell due to the adhesive joint debond when the blade is under fatigue, see Fig. 14 and Supplementary video S1.

Fig. 14. Manufacturing-induced debonds between the shear web and the spar cap at the suction side of the blade. The initial debond is approximately 65cm long and starts 0.5 m from the shear web end, i.e., the debond spans from 1.00 m to 1.65 m along the blade axis. (a) An overview of the adhesive bondline between the shear web and the spar cap. (b) The debond region where a 3- to 5- mm gap exists. (c) An acoustic emission sensor ch #8 is installed close to the crack tip at a 1.65 m blade spanwise location.

DIC measurements

In order to investigate what happened underneath the painted spar cap region at 8.3 m, DIC measurements are carried out. First, it is decided to do DIC measurements under static loading due to a concern of structural collapse under fatigue loading; second, the loading saddle is removed so that the blade has a simple boundary condition as a cantilever beam fixed at the root on the test stand; and then, a static load is applied at the 13 m cross section using a crane that pulls the blade upward. The DIC system measures longitudinal strains along the blade axis direction and transverse strain along the chordwise direction. The DIC measurement results are shown in Fig. 15.

It can be seen that starting from a static load of around 1000 N, the region with the embedded wrinkle WK#2 shows a buckle wave in the spar cap, which is indicated by both compressive longitudinal strains shown in blue and tensile longitudinal strains shown in red in Fig. 15(a). In addition, the discontinuity of strain contour at the top of the winkle region indicates a surface crack there. Note that the buckle covers beyond the spar cap, meaning that the damage has propagated into sandwich panels adjacent to the spar cap.

Fig. 15. Digital Image Correlation (DIC) measurements of strain distributions around the 8.3 m section region. The measurements are taken after the fatigue test. A static load is applied incrementally at the 13 m section of the blade tip. (a) Longitudinal strains along the blade spanwise direction. (b) Transverse strains along the blade chordwise direction. The reference zero strain is set when the blade is not loaded with P=0 N.

To verify the findings from the DIC measurements, the paint is removed and the delamination damage at this location is now visible, see Fig. 16(a). Indeed, the spar cap laminate is significantly damaged by delamination as well as surface cracking. The delamination exists not only in the spar cap but also in the sandwich panels. An endoscope (Teslong TSMS450D8L5 with dual lens) is used to inspect the internal damage of this cross section as shown in Fig. 16 (b). It is shown that the delamination of the inside surface of the spar cap as well as laminate cracking in the shear web. Fig. 16 (c) summarized the internal damage found by the endoscope.

Fig. 16. Fatigue failure at the 8.3m section due to an embedded wrinkle in the spar cap laminate. The observation is made after removing the paint with speckle patterns. (a) Delamination and laminate cracking at the spar cap viewed from the outside surface. (b) Delamination of the spar cap and laminate cracking of the shear web with a view taken from the inside. (c) A schematic illustration of internal damage inspection using an endoscopy through a hole drilled in the aft sandwich panel and the rear shear web.

4.2 Edgewise fatigue

Thermal imaging

After the flapwise fatigue test, the spar cap on the pressure side of the blade has significant delamination damages around the 8.3 m location. Before starting the edgewise fatigue test, tapered scarf repair with wet layup techniques was carried out, see Supplementary material. Thermal images of the blade under edgewise fatigue loading are shown in Fig. 17. The thermal footprint of the wrinkle WK#1 can be seen from Fig. 17(a) although it is not as significant as it was when the blade is under flapwise fatigue. Remarkably, two hot spots are observed *within* the trailing edge debond region TD#1, which will be further examined in the next section. The inboard region of the blade shows thermal footprints of dry areas of skin laminates in the sandwich debond SD#1 as well as the root transition region due to stress concentration, see Fig. 17(b).

Fig. 17. Thermal footprints of damages when the blade is subject to edgewise fatigue loading. (a) Thermal footprints of a wrinkle WK#1 and a trailing edge adhesive debond TD#1. Note that the length of the debond region is longer than the distance between two hot spots marked with cycles within the debond region. (b) Significant thermal abnormity is observed in the dry area of the sandwich debonding SD#1 and in the root transition region. All images are taken when the blade is under fatigue loading.

A few close-up thermal images are taken. Fig. 18(a) shows the thermal features in the inboard region where significant heat up in the suction side spar cap and the root transition region is observed. Visual inspection of these two regions as shown in Fig. 18(b) finds delamination in the root transition region but no damage in the spar cap. It is then decided to take a thermal image from the inside of the blade as shown in Fig. 18(c). It is found out that the thermal feature observed from the spar cap is caused by the thermal activities at the debond in the adhesive bondline between the rear shear web and the suction side spar cap. The thermal activities are due to material rubbing and abrasion in the debond region as shown in Fig. 19. The heat generated in the debonding is so substantial with a detected maximum temperature of 39 ºC in comparison to a surrounding temperature of about 25 ºC that it can be detected from the outside of the blade in the spar cap. This finding shows that it is possible to detect adhesive joint debond underneath the thick spar cap laminate in full-scale blade using thermography without using external heating sources, leading to a new opportunity of using thermography to detect such damages in wind turbine blades while they are in operation.

Fig. 18. Thermal footprints of the shear web debond and the root transition region when the blade is subject to edgewise fatigue loading. (a) A thermal image taken from the suction side of the blade close to the blade root shows two heated regions. One region is the root transition region and the other is the suction side spar cap. (b) An image taken by a regular RGB camera shows two regions with thermal abnormalities. Delamination is found in the root transition region but no damage is found in the suction side spar cap. (c) A thermal image taken inside of the blade shows significant heat-up regions in the adhesive joint between the rear shear web and the suction side spar cap. (d) An RGB camera image shows the bondline under concern. Significant tapping and

rubbing sounds occur during the fatigue loading due to the presence of a debond region there. All images are taken when the blade is under fatigue loading.

Fig. 19. Significant material abrasion is found in the thermal heat-up locations in the adhesive bondline. (a) This image shows location I as indicated in Fig. 18(d). (b) Location II, i.e., the shear web end, as indicated in Fig. 18(d). The images are taken using the endoscope when the cracks are most visible during fatigue loading.

Trailing edge cyclic buckling

Close observation of the trailing edge region TD#1 reveals an interesting phenomenon of cyclic buckling when the blade is subject to edgewise fatigue loading. A Sony FDR-AX53 video camera with a frame rate of 60 FPS is used to capture the local deformation of the trailing edge when the blade moves to the maximum and minimum edgewise direction, see Fig. 20 and Supplementary video S2. It can be seen that the trailing edge region shows considerable buckling waves when it is under compression. Furthermore, it is found that the two locations of wave valleys as indicated in Fig. 20(b) are the ones that generate two hot spots in the thermal images, indicating the matching surfaces of the debond region rub and compress each other, generating heat during the edgewise fatigue as shown in Fig. 20(c). Note that this cyclic buckling phenomenon includes both contact and geometric nonlinearities in the damaged region. A previous study [24] shows that the geometric nonlinearity alone has a significant influence on the fatigue resistance of trailing edge bond lines. With the presence of defects, contact nonlinearity comes into play and further complicates the issue. The importance of including both geometric and contact nonlinearities of trailing edge regions into failure prediction is emphasized in [25], [26]. The new experimental observation found in this study underlines the necessity and the complexity of reliable modeling of nonlinear structural behavior for accurate prediction of local fatigue crack growth in the trailing edge region.

Fig. 20. Cyclic buckling of a trailing edge region with a debond TD#1 under edgewise fatigue loading. (a) The blade moves towards the leading edge direction where the trailing edge is under tension and the trailing edge line is straight. (b) The blade moves towards the trailing edge direction where the trailing edge is under compression and the trailing edge line shows buckling waves. (c) Two matching surfaces of the debond at two wave valleys rub and compress each other, generating two distinct thermal hot spots in the buckling wave. All images are taken when the blade is under fatigue loading. See Supplementary video S2.

Fig. 21. The out-of-plane deformation contour of the trailing edge region is measured by DIC during the edgewise fatigue test. The image is taken when the trailing edge is subject to maximum compression. The reference zero deformation is set when the blade is not loaded. The out-of-plane deformation of a trailing edge line is extracted from the DIC measurements.

DIC measurements

In order to quantify the buckle wave of the trailing edge, DIC measurements are carried out during the edgewise fatigue test. The DIC images are taken for 2 seconds with a sampling rate of 58 Hz. Fig. 21 shows the out-of-plane deformation measured by the DIC, when the trailing edge is subject to maximum compression, i.e., the blade has the maximum displacement towards the trailing edge. A trailing edge cut line is defined to extract the DIC measurement results. The local deformation of the trailing edge line is obtained by subtracting the assumed global deformation from the DIC measurements as shown in Fig. 22. Local out-of-plane deformation is thus 8.1 mm. These deformation values will be used to compare with numerical simulations in a separate study.

Fig. 22. The local out-of-plane deformation of the trailing edge cut line by subtracting the assumed global deformation from the total deformation measured by DIC. It is subsequently obtained that the maximum and minimum amplitudes of the buckling wave is 2.4 and -5.7mm, respectively.

Acoustic emission

The AE emission is rather significant when the blade is loaded at a high load level. Figure 23 shows AE energy activities aligned with strain measurements. The most active AE sensors are ch #1 mounted on the blade root and ch #8 and #9 mounted close to the adhesive joint debond between the rear shear web and the spa cap. The AE sensors ch #8 and #9 are continuously activated by the edgewise loading due to rubbing and tapping of two contacting surfaces, Supplementary video S3. The AE sensor ch #1 captures high energy activities at the same time instants as ch #8 and #9, showing its capability to indicate the overall structural integrity of the blade even though they are mounted far away from the damage location. Although the blade does not fail in the edgewise fatigue test, the high energy AE activities together with an obvious strain range decay start from 23000 s as a result of considerable damage in the blade under edgewise fatigue loading.

Fig. 23. Scatter plots of AE energy show detected activities during the edgewise fatigue loading with two loading levels matching the strain gauge trace. (a) Time history records of strains at 9 m trailing edge (TE) and 10 m leading edge (LE). A high load level loading starts at 14000 s and a strain range decay starts around 23000 s. (b) The overview of AE energy shows considerable AE activities under a high load level particularly in channel #1, #8 and #9. The boom of AE energy activities occurs when the strain range decay starts to appear. (c) A close-up zoom view of (b) with AE energy activities below 600 MARSE.

5. Concluding remarks

This study carried out a comprehensive experimental investigation on fatigue damage growth of a 14.3 m composite wind turbine blade under flapwise and edgewise loading in sequence. The damages are initiated at multiple locations where artificial defects have been embedded in the blade during manufacturing. Damage growths are identified and monitored using a combination of various nondestructive testing and structural health monitoring techniques, i.e., Infrared thermography (IR), Digital Image Correlation (DIC) and Acoustic Emission (AE). By doing so, some new observations shed light on not only damage growth and monitoring of full-scale composite blades but also complex structural nonlinear behavior caused by these damage mechanisms under fatigue. The major findings from this study are highlighted as follows:

(1) Typical damage types were expected to grow in the blade subject to fatigue loading, among them, delamination damages were initiated by the embedded wrinkles in the spar cap laminate and grew steadily before one delamination region eventually failed the blade. The debond of adhesive joints in the trailing edge and between the shear web and the spar cap also grew and caused significant local geometric and contact nonlinearity. The debond between skin laminates and core materials in sandwich panels did not initiate damage growth in this study.

(2) It is shown that thermography effectively detected progressive damage in a full-scale blade under fatigue. This study demonstrated that not only the critical damage such as delamination in the thick spar cap but also the adhesive joint debond underneath the thick spar cap can be detected remotely. Furthermore, local hot spots from a cyclically buckled trailing edge region were also well identified. Remarkably, no external heating source was applied to the blade which heated itself under fatigue and generated thermal abnormities in the damage regions, providing a real-time and large-area monitoring solution for the blades under fatigue.

(3) This study also demonstrated the application of DIC to measure a trailing edge region of a full-scale blade under fatigue loading, revealing the first-of-its-kind experimental observation of cyclic buckling when the trailing edge has an adhesive joint debond. This finding has significant implications for fatigue modeling and prediction, showing that both geometric and contact nonlinearities have to be taken into account when predicting fatigue crack growth with the presence of damage in the trailing edge bondline.

(4) Continuous AE measurements were able to indicate imminent critical structural failure. The AE sensor placed on the spar cap monitored the overall structural integrity of the blade even though it was located close to the blade root and therefore far away from the precise failure location. The deployment of an AE sensor at the root of the blade was proved to be an effective instrumentation strategy to monitor the overall structural integrity of the blades.

(5) The decay of strain range during the fatigue test was caused by the change of dynamic properties, i.e., natural frequencies and/or mode shapes of the blade subject to resonance-based fatigue loading. The strain

decay phenomenon reflected the overall damage accumulation of the blade due to the stiffness loss, however, it was not a reliable indication of imminent critical structural failure. In hindsight, we should have realized in the flapwise fatigue loading that the decay of strain range was related to an important loss of stiffness emerging from the onset of structural failure.

(6) The tapping and rubbing of the two matching surfaces due to the adhesive joint debond between the shear web and the spar cap manifested contact nonlinearity of local structural details in blade structures. This observation addresses the necessity as well as the complexity of reliable modeling and prediction of nonlinear structural behavior on a large scale in order to predict local fatigue crack growth.

This work only focused on experimental investigations. More studies have to be done in order to fully unveil the underlying failure mechanisms and their implications to design, modeling and testing of composite blades. Further studies following this work will include fractographic analysis of the damaged regions using X-ray computed tomography (CT) and a Scanning Electron Microscope (SEM) to get insights into failure mechanisms; numerical modeling of fatigue damage growth in spar cap laminates and adhesive bond lines such as using the recently developed FASTIGUE approach [27]; biaxial fatigue testing of a second blade which has embedded with the same artificial defects as the one presented in this study. Moreover, integrated imaging techniques using thermoelastic stress analysis (TSA) and DIC [28][29] will be used in the future blade test to offer more insights into damage behavior over a large range of length and time scales. The recently developed AQUADA method [30] will be also used in the future study to automatically quantify the damage status of composite rotor blades under operational fatigue loads using thermography and computer vision.

Acknowledgments

References:

[1]   International Electrotechnical Commission, "IEC Standard 61400-23, Wind Turbines – Part 23: Full-scale Structural Testing of Rotor Blades, Edition 1.0." International Electrotechnical Commission, 2014.

[2]   J. B. Jørgensen, B. F. Sørensen, and C. Kildegaard, "Tunneling cracks in full scale wind turbine blade joints," *Eng. Fract. Mech.*, vol. 189, pp. 361–376, 2018, doi: 10.1016/j.engfracmech.2017.11.016.

[3]   H. G. Lee, M. G. Kang, and J. Park, "Fatigue failure of a composite wind turbine blade at its root end," *Compos. Struct.*, vol. 133, pp. 878–885, 2015, doi: 10.1016/j.compstruct.2015.08.010.

[4]   O. Al-Khudairi, H. Hadavinia, C. Little, G. Gillmore, P. Greaves, and K. Dyer, "Full-scale fatigue testing of a wind turbine blade in flapwise direction and examining the effect of crack propagation on the blade performance," *Materials (Basel).*, vol. 10, no. 10, 2017, doi: 10.3390/ma10101152.

[5]   X. Chen, "Experimental observation of fatigue degradation in a composite wind turbine blade," *Compos. Struct.*, vol. 212, 2019, doi: 10.1016/j.compstruct.2019.01.051.

[6]   X. Chen, "Fracture of wind turbine blades in operation—Part I: A comprehensive forensic investigation," *Wind Energy*, vol. 21, no. 11, 2018, doi: 10.1002/we.2212.

[7]   M. Leong, L. C. T. Overgaard, O. T. Thomsen, E. Lund, and I. M. Daniel, "Investigation of failure mechanisms in GFRP sandwich structures with face sheet wrinkle defects used for wind turbine blades," *Compos. Struct.*, vol. 94, no. 2, pp. 768–778, 2012, doi: 10.1016/j.compstruct.2011.09.012.

[8]   J. F. Mandell, D. S. Cairns, D. D. Samborsky, R. B. Morehead, and D. J. Haugen, "Prediction of delamination in wind turbine blade structural details," *J. Sol. Energy Eng. Trans. ASME*, vol. 125, no. 4, pp. 522–530, 2003, doi: 10.1115/1.1624613.

[9]   D. S. Cairns, T. Riddle, and J. Nelson, "Wind Turbine Composite Blade Manufacturing : The Need for Understanding Defect Origins , Prevalence , Implications and Reliability," 2011. [Online]. Available: http://www.ntis.gov/help/ordermethods.asp?loc=7?4?0#online.

[10]   J. J. Bender, S. R. Hallett, and E. Lindgaard, "Investigation of the effect of wrinkle features on wind turbine blade sub-structure strength," *Compos. Struct.*, vol. 218, no. March, pp. 39–49, 2019, doi: 10.1016/j.compstruct.2019.03.026.

[11]   J. J. Bender, S. R. Hallett, and E. Lindgaard, "Parametric study of the effect of wrinkle features on the strength of a tapered wind turbine blade sub-structure," *Compos. Struct.*, vol. 218, no. February, pp. 120–129, 2019, doi: 10.1016/j.compstruct.2019.02.065.

[12]   K. M. Jespersen and L. P. Mikkelsen, "Three dimensional fatigue damage evolution in non-crimp glass fibre fabric based composites used for wind turbine blades," *Compos. Sci. Technol.*, vol. 153, pp. 261–272, 2017, doi: 10.1016/j.compscitech.2017.10.004.

[13]   M. McGugan, G. Pereira, B. F. Sorensen, H. Toftegaard, and K. Branner, "Damage tolerance and structural monitoring for wind turbine blades," *Philos. Trans. R. Soc. A Math. Phys. Eng. Sci.*, vol. 373, no. 2035, 2015, doi: 10.1098/rsta.2014.0077.

[14]   M. Desmond, S. Hughes, and J. Paquette, "Structural Testing of the Blade Reliability Collaborative Effect of Defect Wind Turbine Blades Structural Testing of the Blade Reliability Collaborative Effect of Defect Wind Turbine Blades," National Renewable Energy Laboratory, Golden, CO, USA, 2015.

[15]   C. Niezrecki *et al.*, "Inspection and monitoring of wind turbine blade-embedded wave defects during fatigue testing," *Struct. Heal. Monit.*, vol. 13, no. 6, pp. 629–643, 2014, doi: 10.1177/1475921714532995.

[16]   M. A. Rumsey and J. A. Paquette, "Structural health monitoring of wind turbine blades," *Smart Sens. Phenomena, Technol. Networks, Syst. 2008*, vol. 6933, no. April 2008, p. 69330E, 2008, doi: 10.1117/12.778324.

[17]   X. Chen *et al.*, "Standard Static Tests of a 14.3 m Olsen Wing Blade: A project report of BLATIGUE funded by EUDP," DTU Wind Energy, 2018.

[18]   Bladena and KIRT x THOMSEN, *Wind Turbine Blades Handbook - A shared lingo of terms and definitions for wind turbine blades*. 2019.

[19]   O. T. Thomsen, "Sandwich materials for wind turbine blades - Present and future," *J. Sandw. Struct. Mater.*, vol. 11, no. 1, pp. 7–26, 2009, doi: 10.1177/1099636208099710.

[20]   A. G. Beattie and M. Rumsey, "AIAA 99-0046 Evaluation of Wind Turbine Blades Using an Infrared Camera," *Am. Inst. Aeronaut. Astronaut.*, pp. 1–8, 1999.

[21]   O. J. D. Kristensen and E. R. Jorgensen, "Accelerated fatigue testing of LM 19.1 blades," Risø National Laboratory, Denmark, 2003.

[22]   B. LeBlanc, C. Niezrecki, P. Avitabile, J. Chen, and J. Sherwood, "Damage detection and full surface characterization of a wind turbine blade using three-dimensional digital image correlation," *Struct. Heal. Monit.*, vol. 12, no. 5–6, pp. 430–439, 2013, doi: 10.1177/1475921713506766.

[23]   M. Simonsen, "Speckle Generator." http://www.correlatedsolutions.com/support/index.php?/Knowledgebase/Article/View/19/13/speckle-generator (accessed Jul. 20, 2020).

[24]   P. N. Castelos and C. Balzani, "The impact of geometric non-linearities on the fatigue analysis of trailing edge bond lines in wind turbine rotor blades," *J. Phys. Conf. Ser.*, vol. 749, no. 1, 2016, doi: 10.1088/1742-6596/749/1/012009.

[25]   X. Chen, P. U. Haselbach, K. Branner, and S. H. Madsen, "Effects of different material failures and surface contact on structural response of trailing edge sections in composite wind turbine blades," *Compos. Struct.*, vol. 226, no. August, p. 111306, 2019, doi: 10.1016/j.compstruct.2019.111306.

[26]   X. Chen, P. Berring, S. H. Madsen, K. Branner, and S. Semenov, "Understanding progressive failure mechanisms of a wind turbine blade trailing edge section through subcomponent tests and nonlinear FE

analysis," *Compos. Struct.*, vol. 214, 2019, doi: 10.1016/j.compstruct.2019.02.024.

[27] M. A. Eder and X. Chen, "FASTIGUE: A computationally efficient approach for simulating discrete fatigue crack growth in large-scale structures," *Eng. Fract. Mech.*, vol. 233, no. December 2019, p. 107075, 2020, doi: 10.1016/j.engfracmech.2020.107075.

[28] J. Dulieu-Barton, "Integrating imaging techniques for assessing the performance of large composites structures," in *ICCM 22*, 2019, pp. 1105–1113, [Online]. Available: https://search.informit.com.au/documentSummary;dn=862954502231942;res=IELENG.

[29] J. Dulieu-Barton and O. T. Thomsen, "TOWARDS A NEW PARADIGM FOR HIGH- MULTI-SCALE MODELLING OF COMPOSITE SUBSTRUCTURES AND COMPONENTS," in *2nd International Symposium on Multiscale Experimental Mechanics*, 2017, no. ISMEM, pp. 8–9.

[30] Xiao Chen, ASM Shihavuddin, Kenneth Thomsen, Steffen Rasmussen, Kim Branner, AQUADA: Automated Quantification of Damages in Composite Wind Turbine Blades for LCOE Reduction. Wind Energy. DOI: https://doi.org/10.1002/we.2587
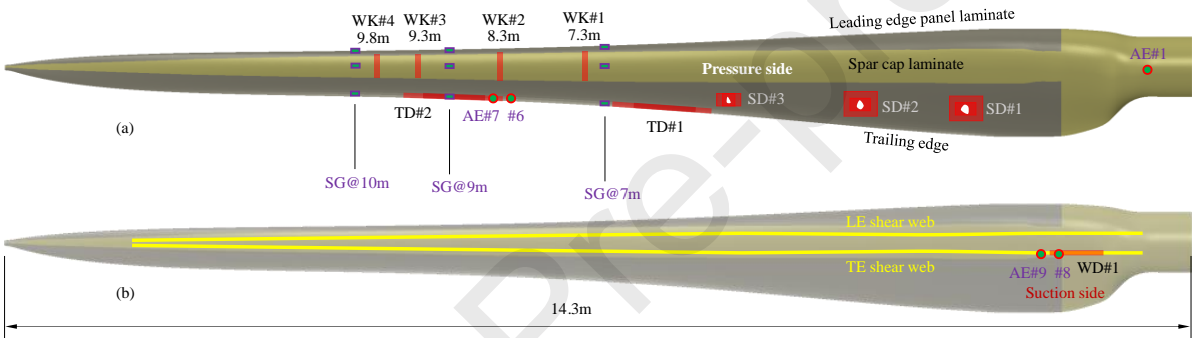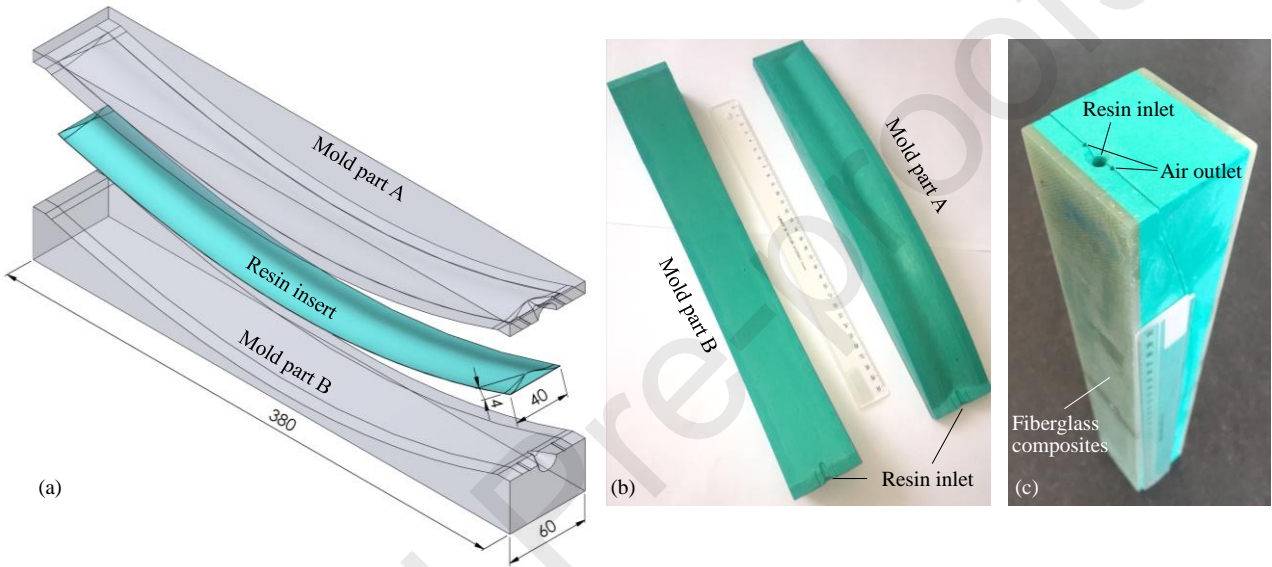
Figure 1

Figure 2

Figure 3

Figure 4

IR camera

Scaffold tower

(a)

DIC cameras

Loading saddle

Biaxial fatigue exciter

(b)
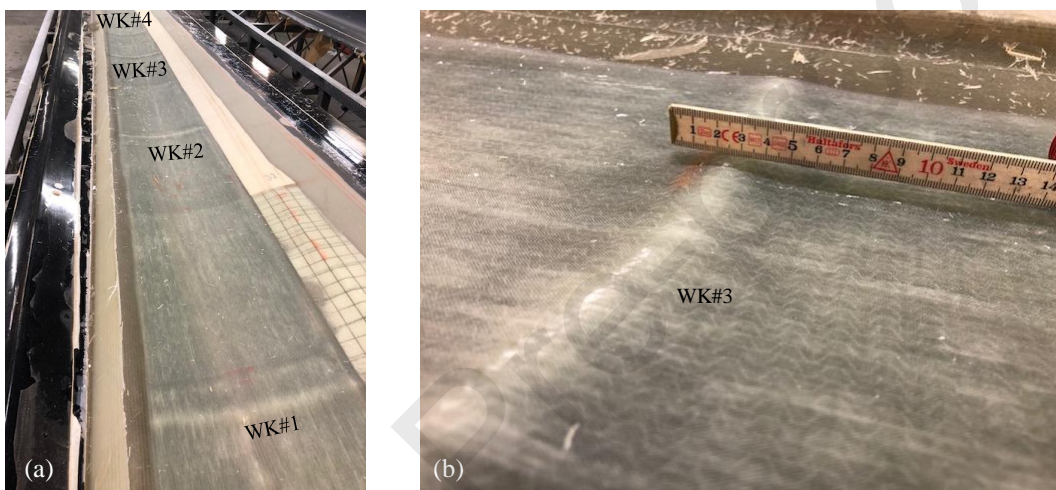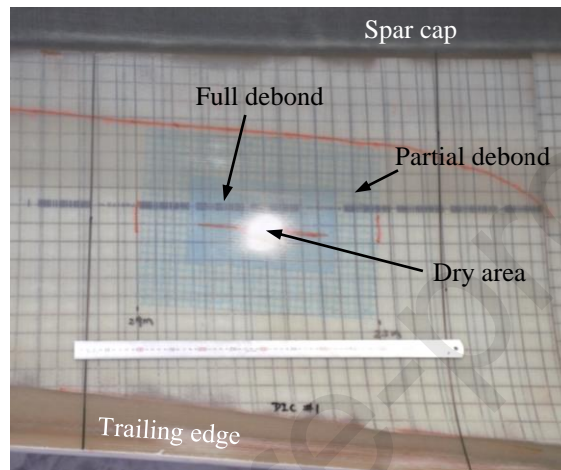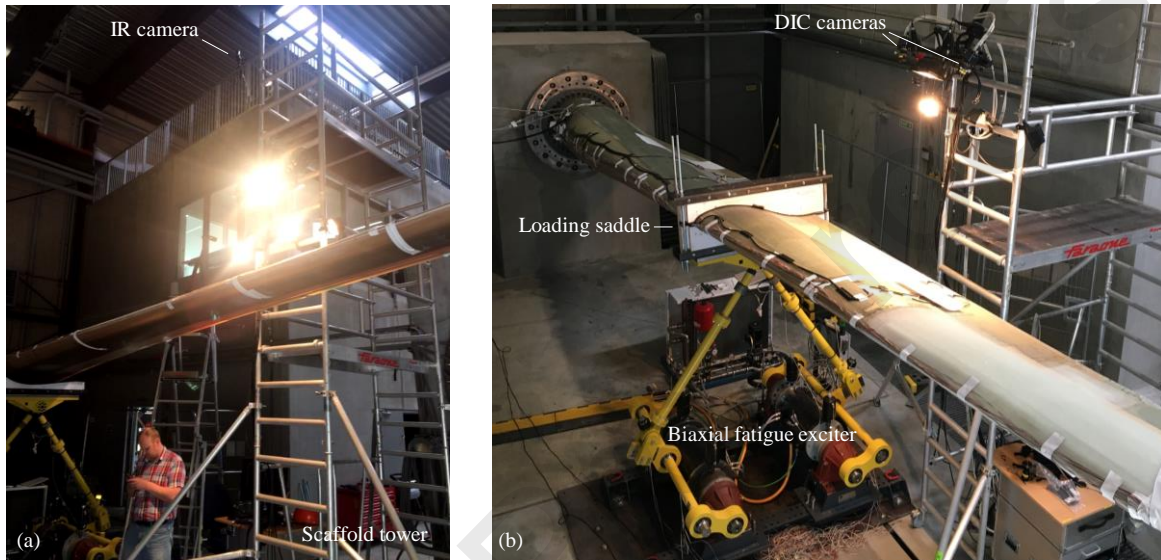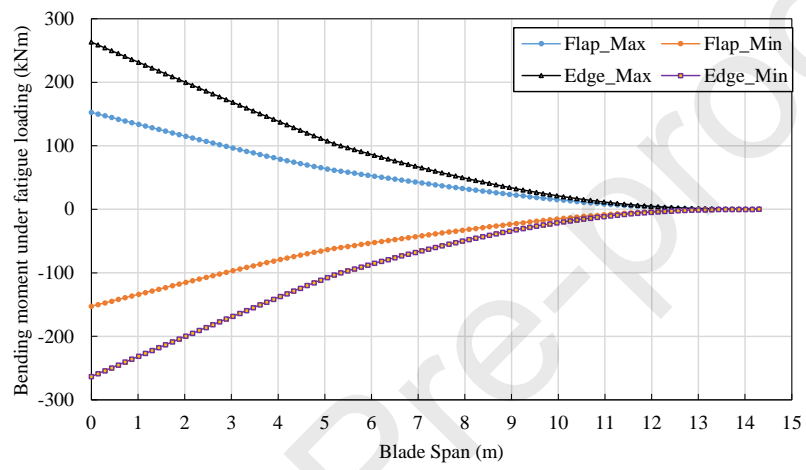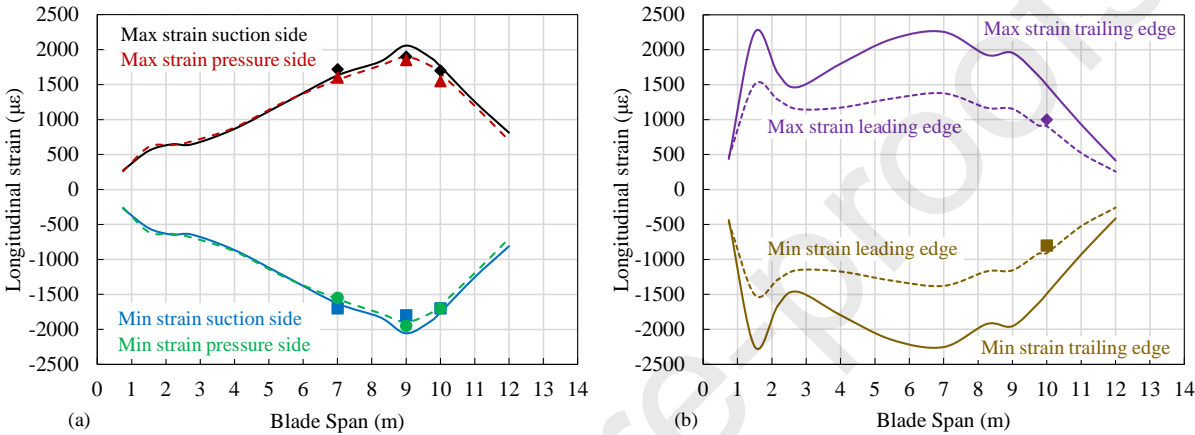
Figure 5

Figure 6

Figure 7
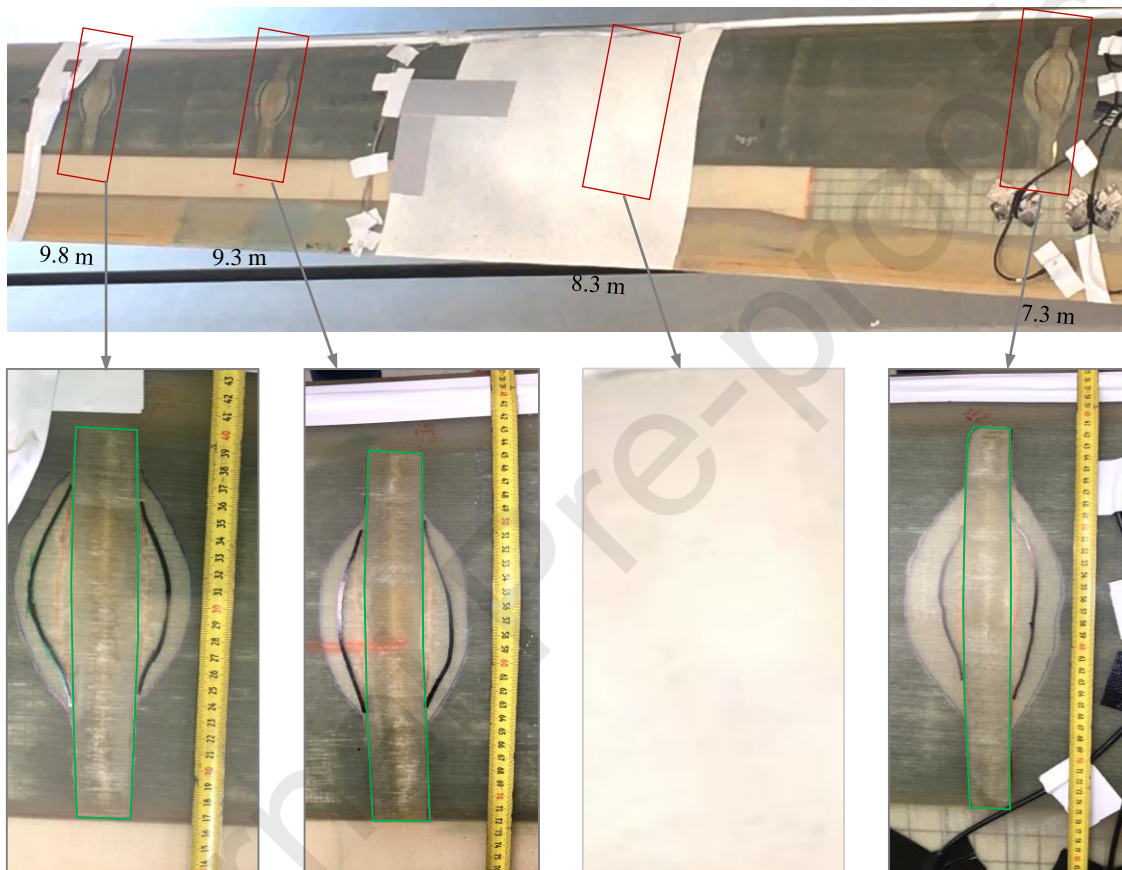
Figure 8
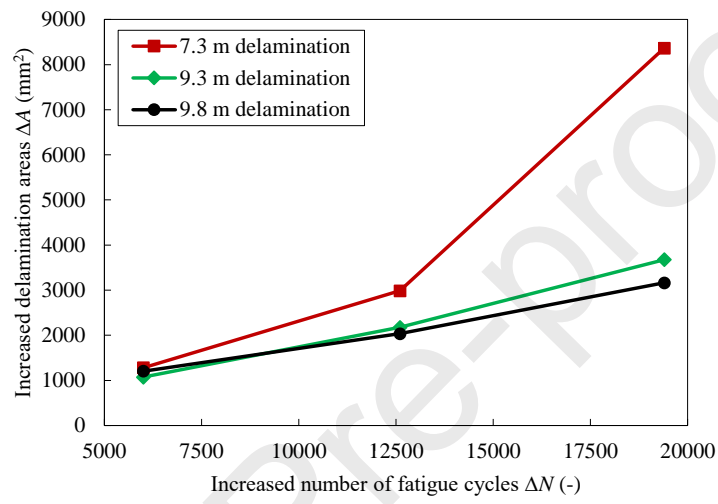
Figure 9
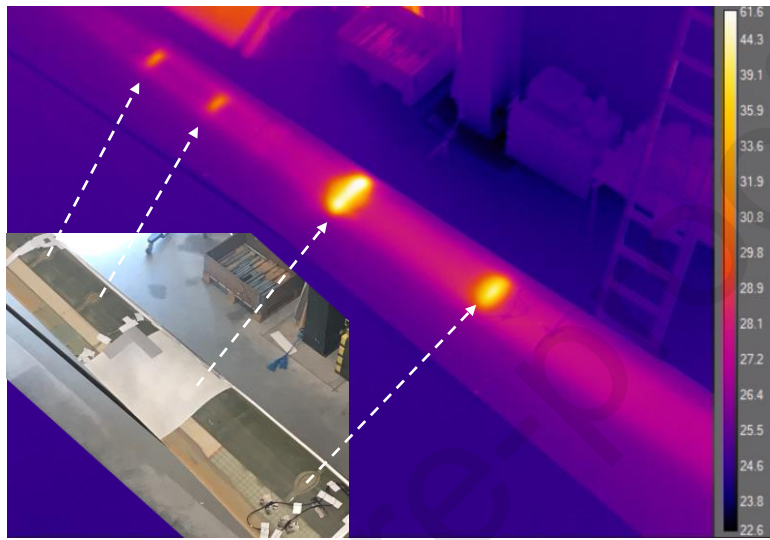
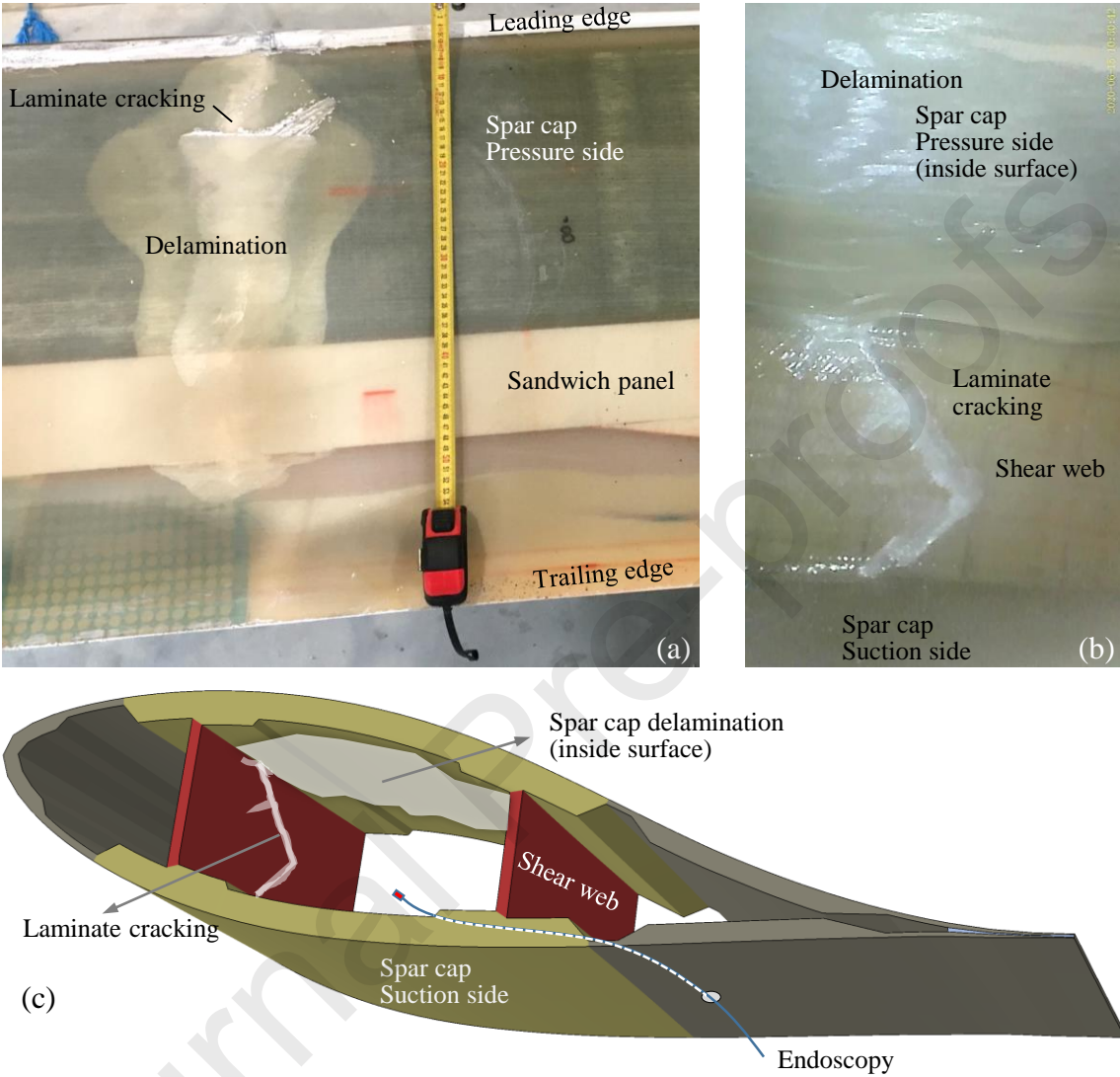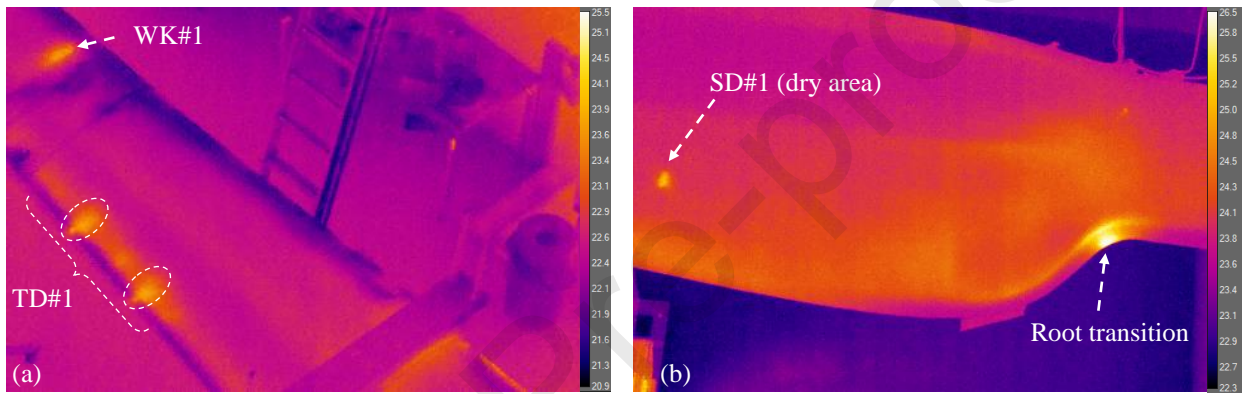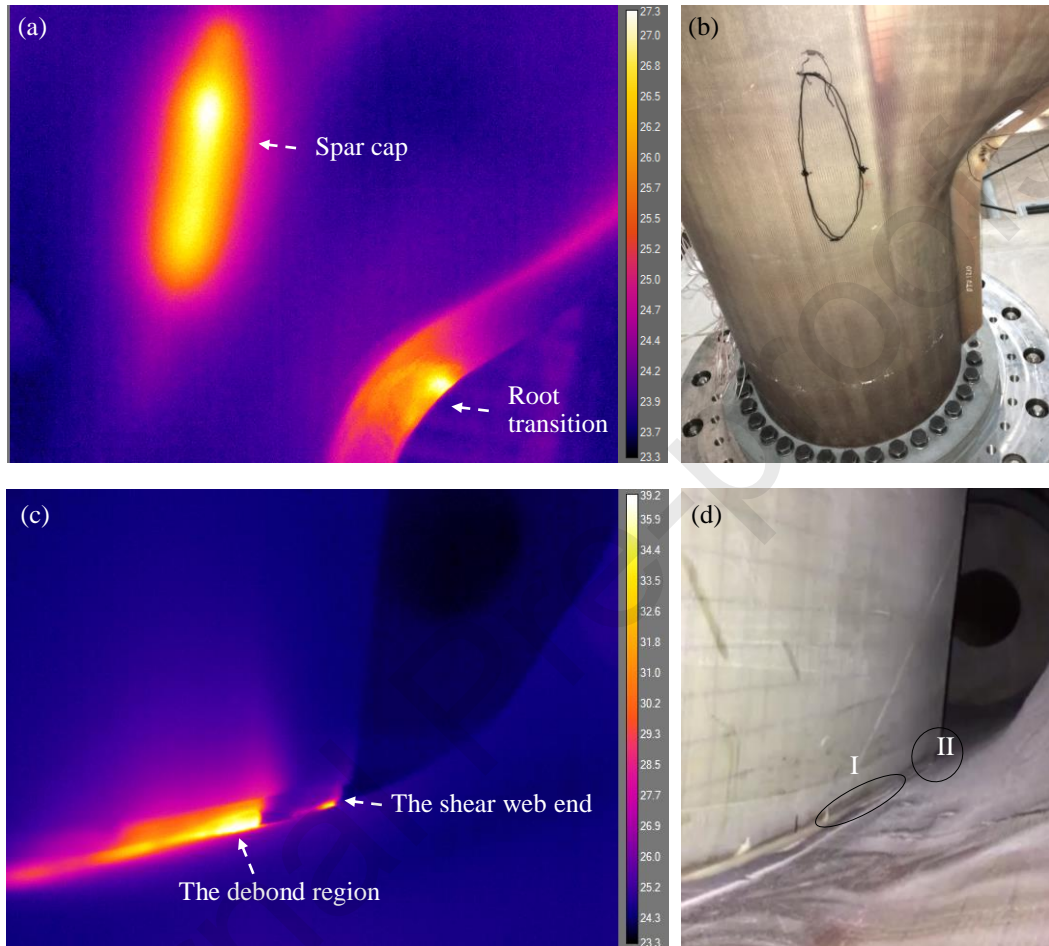Figure 10
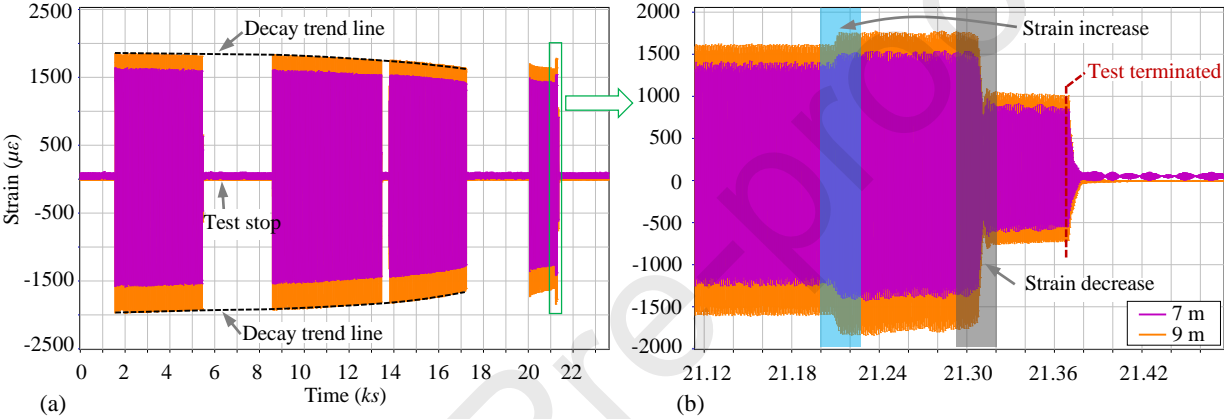
Figure 11
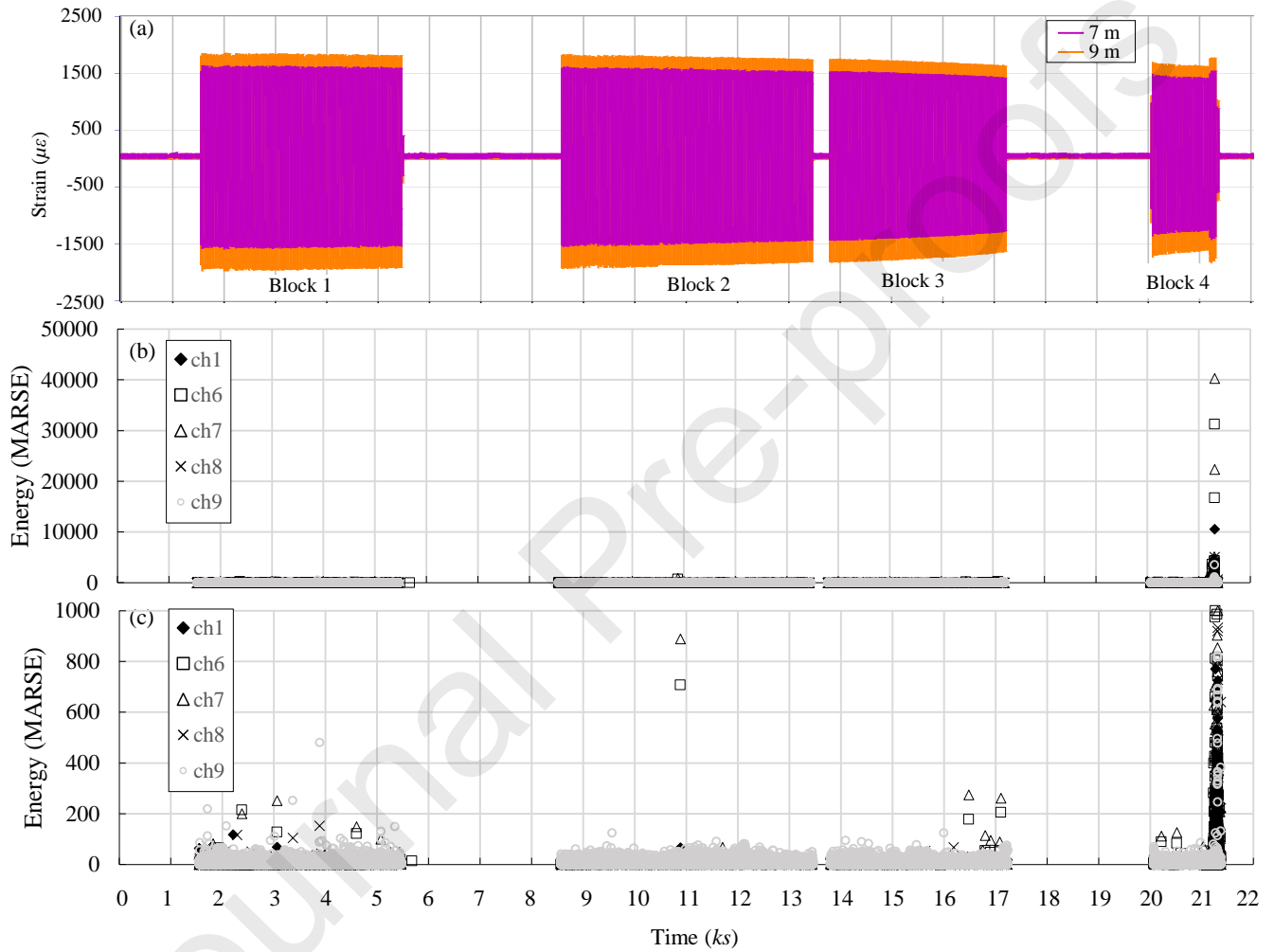
Figure 12
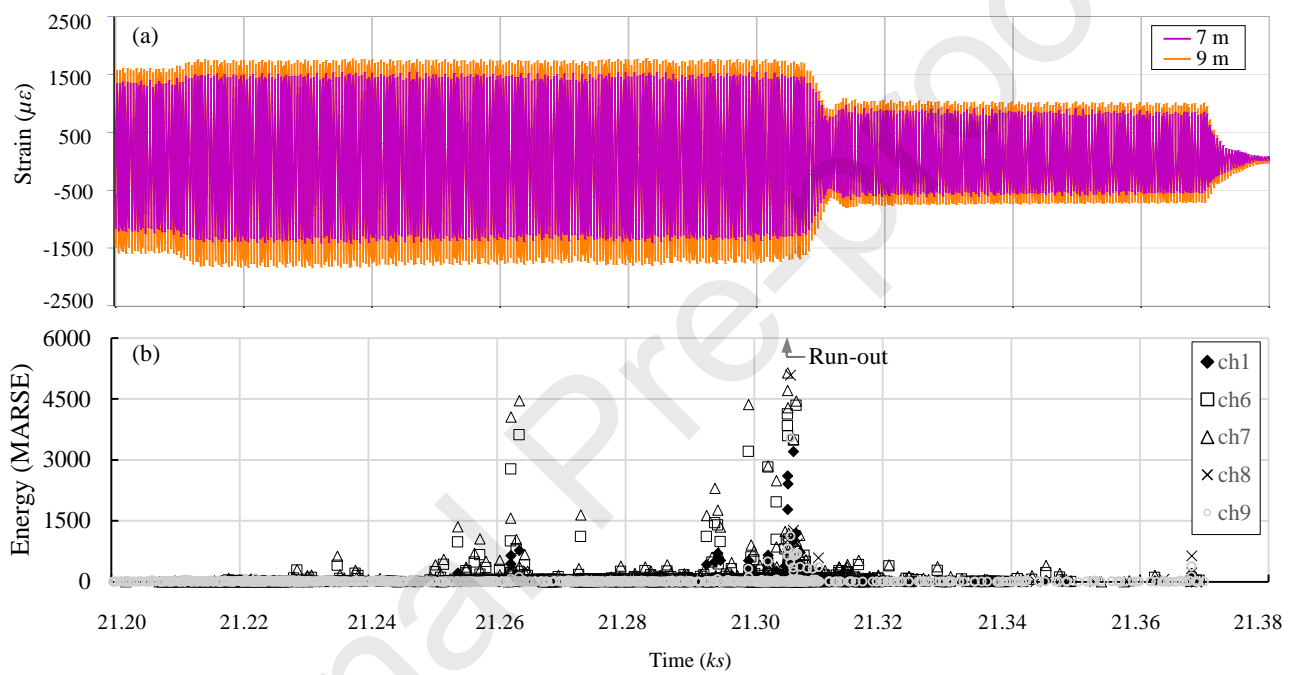
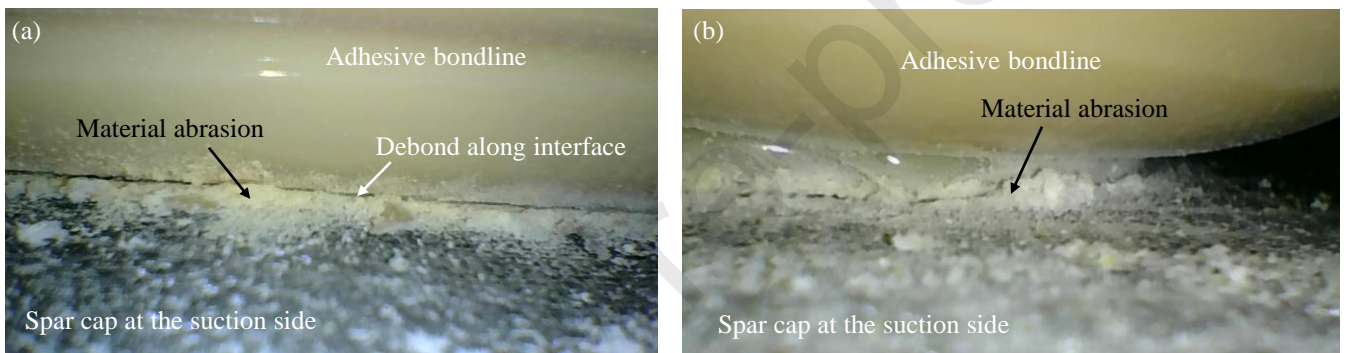Figure 13

Figure 14

(a)

(b)
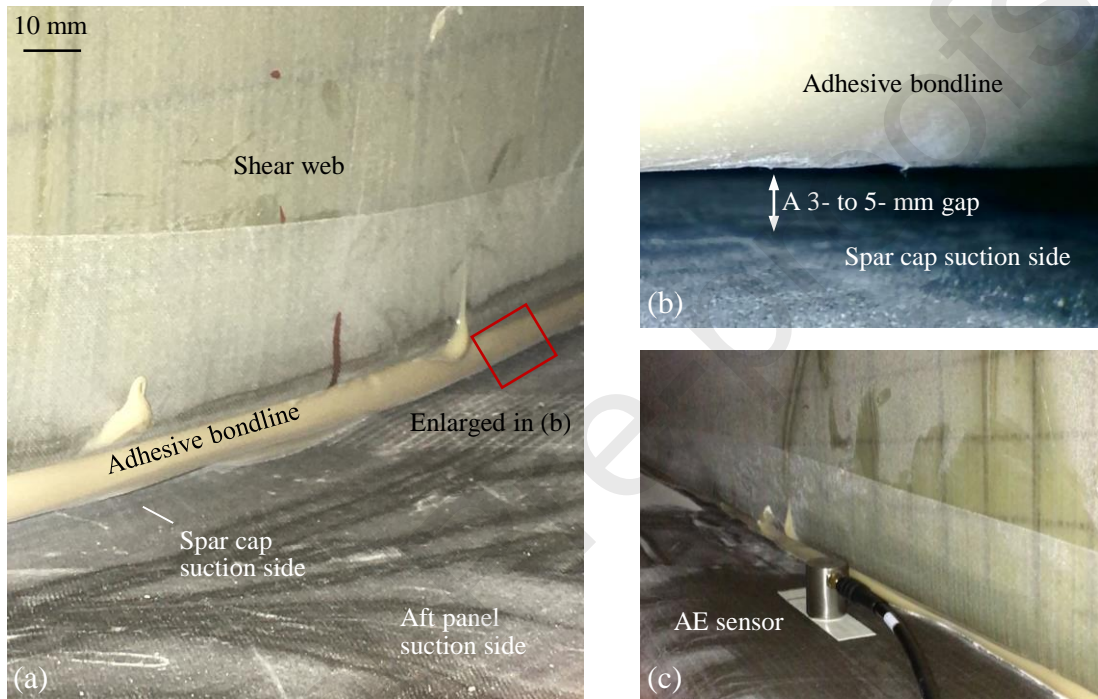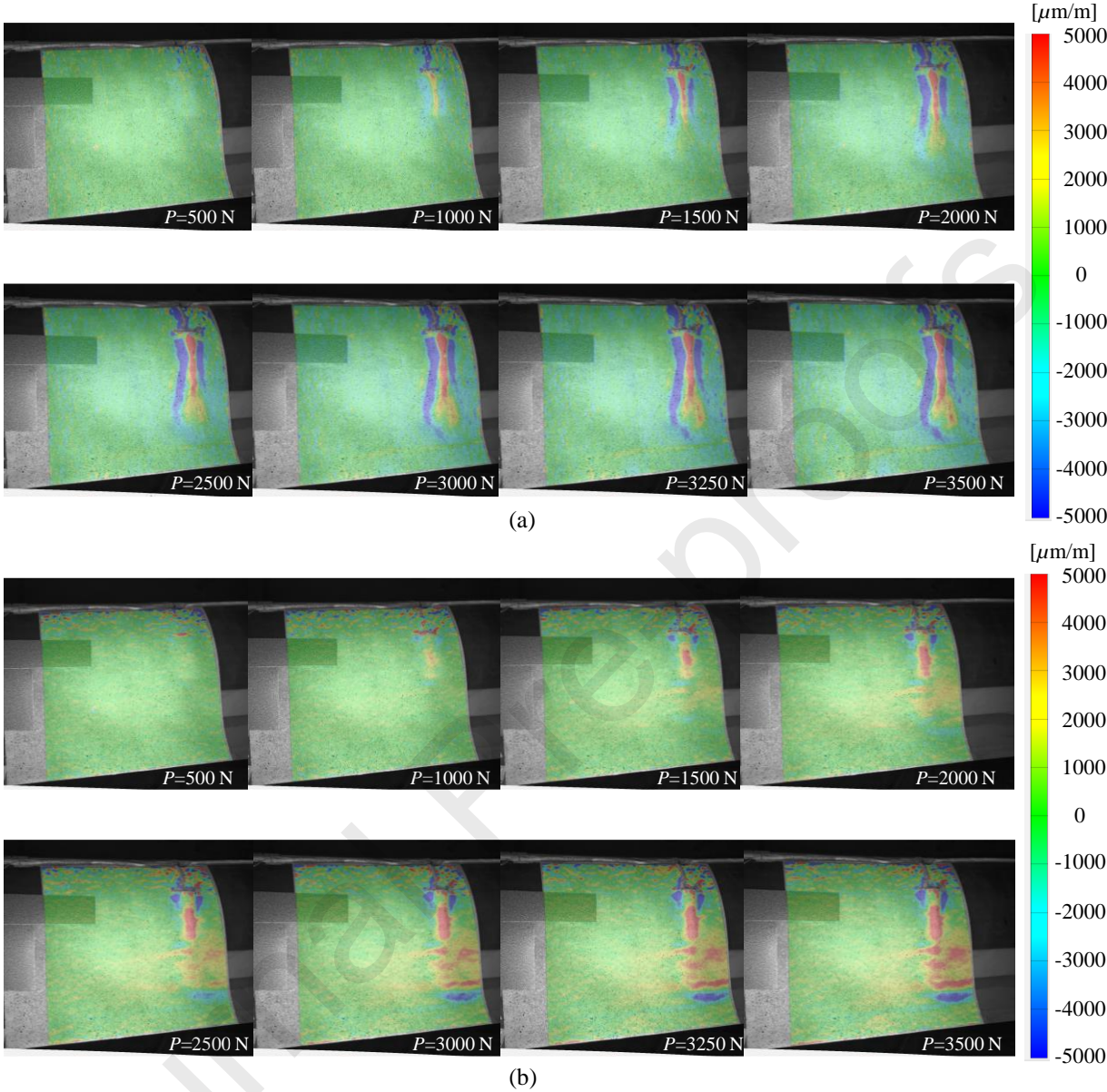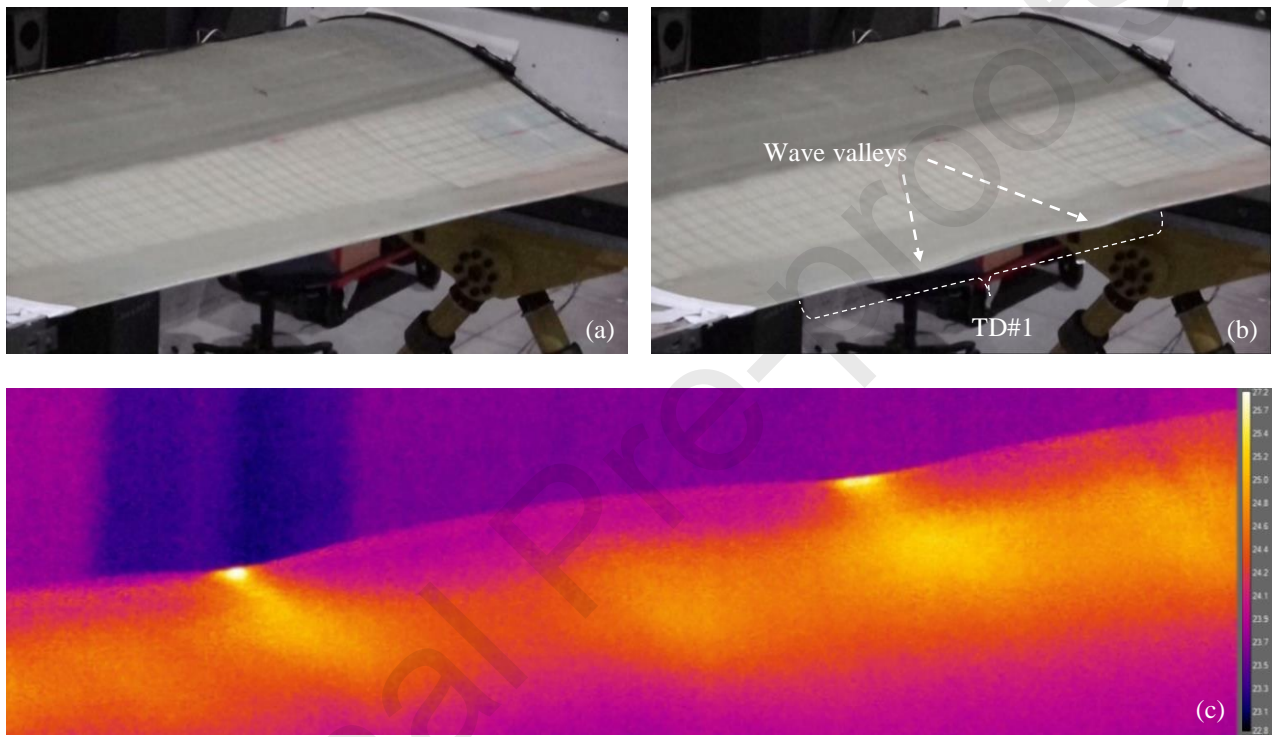
Figure 15

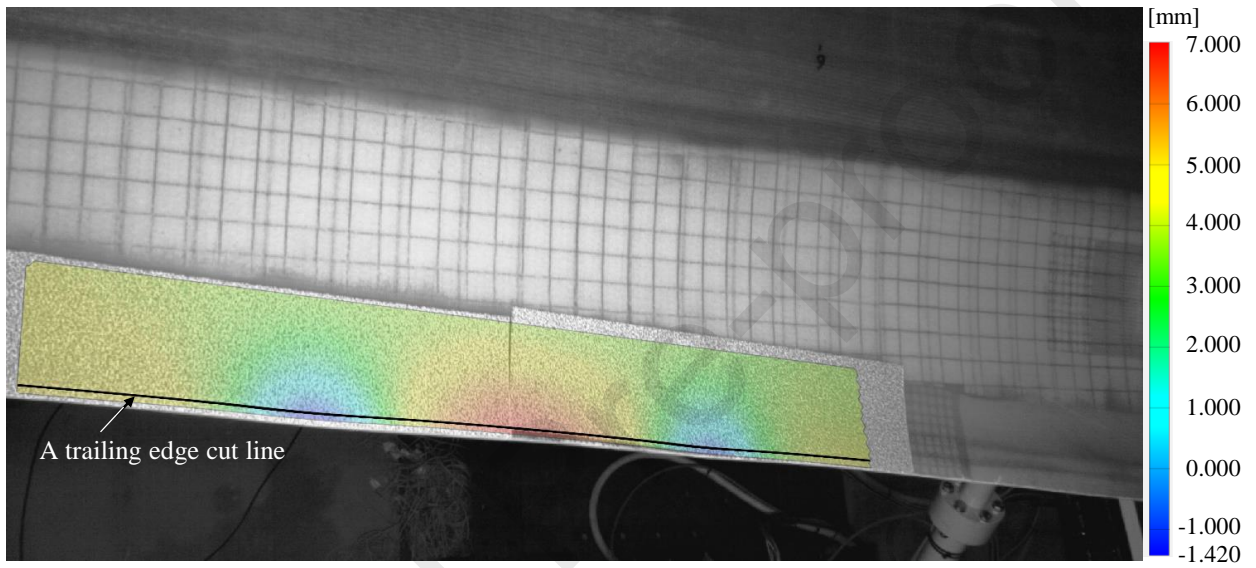Figure 16

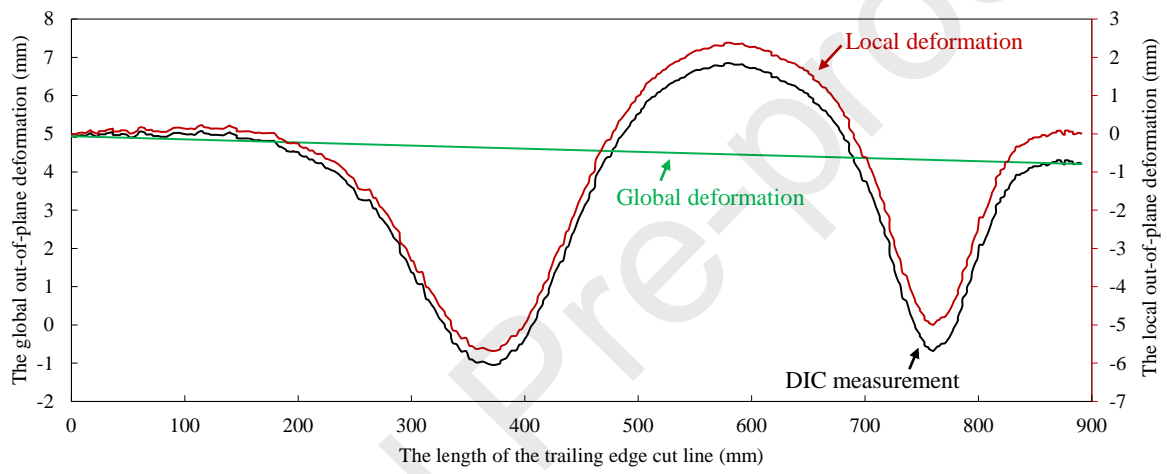Figure 17
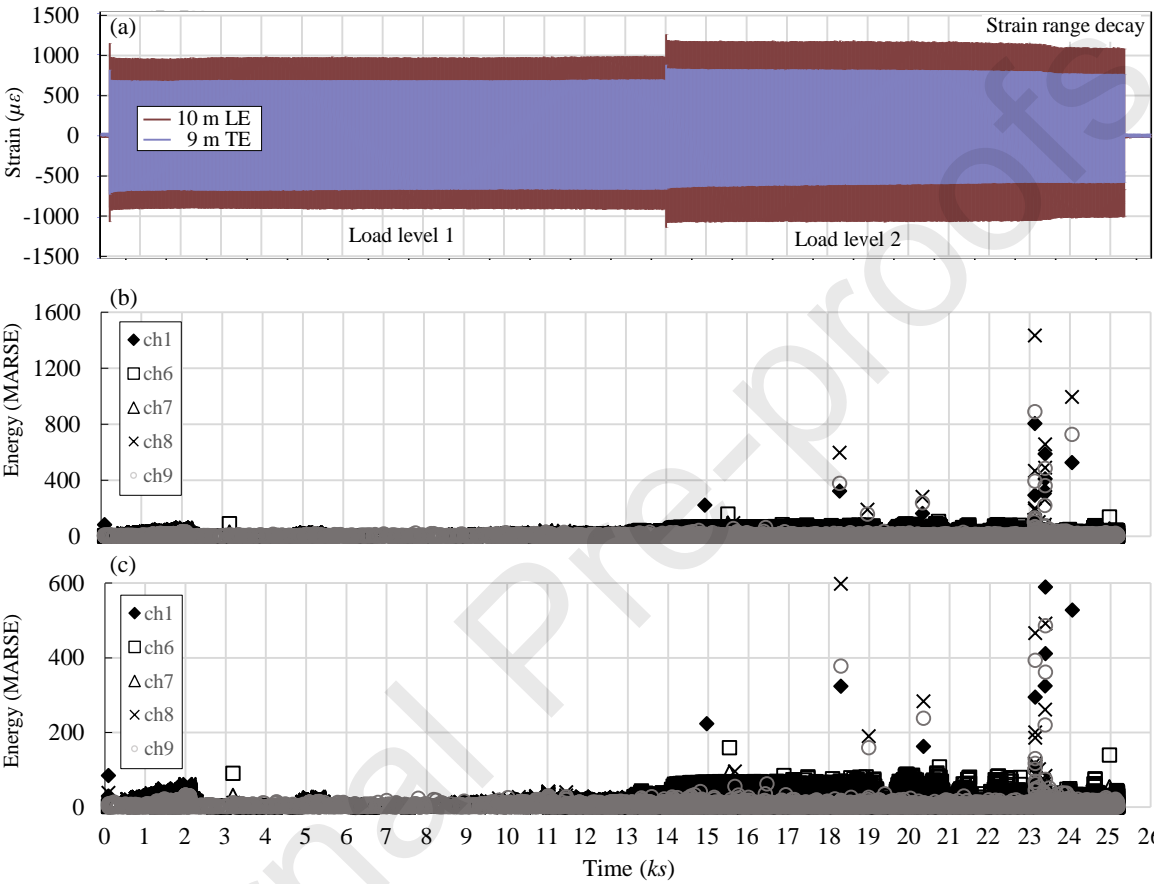
Figure 18

Figure 19

Figure 20

Figure 21

Figure 22

Figure 23

- Fatigue damage growth of a full-scale composite wind turbine blade with artificial defects.

- Real-time, large-area, remote damage detection and monitoring under fatigue loading.

- New nonlinear structural phenomena important for modeling fatigue damage growth.

- Laboratory demonstration facilitates effective SHM application in the field.

The authors declare to have NO competing interests or any conflict of interest.

Author contributions

X.C. conceived the research. X.C. designed and carried out the blade test together with S.S. and S.H.M. X.C. and M.M. collected and analyzed the AE data. S.C.Y. performed load calculation. X.C. and P.B. designed defects together. K.B. provided valuable comments to this work and acquired funding to support this study. X.C. wrote the manuscript and prepared all figures. All authors reviewed the manuscript.